Efficient OFDM Signaling Schemes For Visible Light Communication Systems

EFFICIENT OFDM SIGNALING SCHEMES FOR VISIBLE LIGHT COMMUNICATION SYSTEMS

BY

KASRA ASADZADEH, B.Sc.

A THESIS

SUBMITTED TO THE DEPARTMENT OF ELECTRICAL & COMPUTER ENGINEERING

AND THE SCHOOL OF GRADUATE STUDIES

OF MCMASTER UNIVERSITY

IN PARTIAL FULFILMENT OF THE REQUIREMENTS

FOR THE DEGREE OF

MASTER OF APPLIED SCIENCE

Master of Applied Science (2011) McMaster University

(Electrical & Computer Engineering) Hamilton, Ontario, Canada

TITLE:	Efficient OFDM Signaling Schemes For Visible Light Communication Systems
AUTHOR:	Kasra Asadzadeh B.Sc., (Electrical Engineering) Sharif University of Technology, Tehran, Iran
SUPERVISOR:	Dr. Steve Hranilovic
NUMBER OF PAGES:	xiii, 99

To my parents who dedicated their life to their children

Abstract

Solid-state LED lighting is a promising technology to improve the energy efficiency of general illumination. The inherent modulation bandwidth of these devices can be exploited to provide a dual role as a communication device. This method of communication is termed visible light communications (VLC).

Due to dispersive nature of the VLC channel, orthogonal frequency division multiplexing (OFDM) has been proposed to allow multi-user communication while mitigating the effects of inter-symbol interference (ISI). However, OFDM is in general not compatible with intensity modulation and direct detection (IM/DD) channels since it has both positive and negative amplitudes. Various techniques have been proposed that provide compatible optical OFDM signaling such as DC-biased OFDM, asymmetrically clipped optical OFDM (ACO-OFDM), and pulse amplitude modulated discrete multi-tone (PAM-DMT).

This thesis develops spectrally factorized optical OFDM (SFO-OFDM) as a framework to implement OFDM on optical intensity channels. The drawbacks of conventional methods are mitigated in SFO-OFDM. Contrary to ACO-OFDM and PAM-DMT, the proposed technique uses all the available bandwidth for data modulation and does not require reserved subcarriers. Simulation results verify that SFO-OFDM has gain both in optical power efficiency and peak-to-average power ratio compared

to conventional optical OFDM schemes.

Furthermore in this thesis, a new receiver design for ACO-OFDM and PAM-DMT is proposed. Unlike conventional receivers that ignore the structure of the transmitted signal, the new detector exploits this structure to improve the optical power efficiency. By observing the time domain samples, a simple pairwise maximum likelihood detector is developed and used to remove half of the noise power. It is also shown by simulation results that employing the proposed detector design leads to a significant gain in optical power efficiency.

Acknowledgements

First and foremost, I offer my sincerest gratitude to my supervisor, Dr. Steve Hranilovic, whose advice and support guided me thoughout my research. I attribute the level of my Masters degree to his encouragement and effort. One simply could not wish for a better or friendlier supervisor.

I would also like to express my deepest thanks to all my friends especially my lab mates, who provided a perfect environment for my studies and research.

Last but not least, I would like to express my heartily gratitudes to my family for their unconditional support and love.

Contents

List of Figures

Chapter 1

Introduction

Wireless optical technology provides various outdoor and indoor services such as indoor wireless infrared communications [1], terrestrial links [2], wireless ultraviolet communications [3], and visible light communications [4]. The latter case uses visible light (wavelengths of 380-750 nanometers [5]) as the medium for data transmissions. In this case, an additional advantage lies in the potential for simultaneous use of light for illumination and data communication termed visible light communications (VLC).

Solid state lighting (SSL) refers to a type of lighting that uses semiconductor light emitting diodes (LEDs) as a source of illumination rather than electrical filaments (used in incandescent halogen light bulbs) or plasma (used in fluorescent lamps). Recent developments in LED technology are paving the way towards its full adoption as a replacement to incandescent and fluorescent lighting and white LEDs are now considered as future lighting solutions [6, 7]. Sales of inefficient incandescent light bulbs will be outlawed in Ontario and California beginning in 2012. Australia has announced a similar ban beginning in 2010 and inefficient incandescent bulbs are no

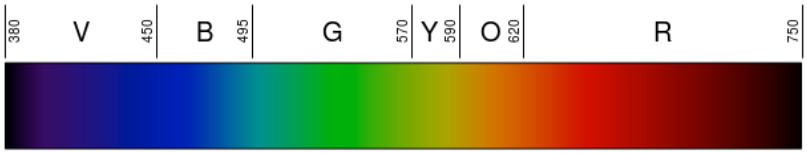

Figure 1.1: The visible spectrum corresponding to: 380-450 nm violet, 450-495 nm blue, 495-570 nm green, 570-590 nm yellow, 590-620 nm orange, and 620-750 nm red region [5].

longer in Europe as of 2009. Surveys in [8, 9] compare LEDs versus incandescent light bulbs and fluorescent lamps in terms of lifetime, efficiency, reliability and cost. One of the main advantages of LEDs over other lighting methods is their longer lifetime expectancy. The average life span of an LED is about 60 kilohours which is considerably more than average lifetime expectancy of incandescent bulbs (about 1200 hours) and fluorescent lamps (about 10 kilohours). Other than that, LEDs are considered more energy efficient as they only consume about 6 W, which is 10% of the power used by incandescent bulbs (about 60 W), and 40% of that used by fluorescent lamps (about 14 W) per unit of light generated (lumen [lm]) [8]. Although the cost of a single LED bulb is more than an incandescent bulb or a fluorescent lamp (approximately \$16 for LEDs made by STARLIGHT INC. compared to \$1.25 and \$3 for incandescents and fluorescents respectively [9]), the total cost of employing LEDs in terms of operating hours and installations is much less than employing other two methods. For example, if the electricity cost is estimated about \$0.2 per kWh, the total cost of employing LEDs for 60 kilohours operation is estimated around \$88 which is considerably less than that for incandescent lights (\$783) and fluorescent lamps (\$186) [9]. As a result, LEDs are more economical for lighting purposes.

Fluorescent lamps contain toxic mercury that can be released if broken. Both incandescent light bulbs and fluorescent lamps suffer from their sensitivity to low

temperatures and humid weathers [8]. Hence, LEDs have less environmental impact and higher reliability in comparison to incandescent bulbs and fluorescents. However, the efficiency with which LEDs produce light degrades with heating effects. Furthermore, the LEDs' brightness is limited per LED and sufficient number of LEDs are required for brightness of the area.

Apart from lighting advantages, LEDs can be modulated at rates greater than several hundred thousands times that of incandescent or fluorescent sources and hence offer the potential for data communication concurrent with lighting [10].

1.1 Current State of VLC, Standardizations and Challenges

Visible light communications was pioneered in Japan [11, 12, 13] but there is now a growing interest in Europe, namely the hOME Gigabit Access (OMEGA) project [14, 15, 16], and USA [17, 18], namely Boston Smart Lighting Center [19].

In order to have widespread adoption, VLC technology must be standardized. Today, there exist several Japanese standards such as Japan Electronics and Information Technology Industries Association (JEITA) [20, 21, 22]. The first standard JEITA CP-1221 restricts the wavelength of all emissions to be within the range of 380 nm to 750 nm with an accuracy of 1 nm per application. For example, if an application claims to send light within 450 nm to 500 nm, emitted wavelengths must be between 449 nm to 501 nm. Unlike this standard, JEITA CP-1222 is supposed to be only used for communications. It includes some restrictions in the frequency used and modulation schemes. There is also an ongoing work to develop VLC standards

within IEEE (IEEE 802.15) [23]. The IEEE has formed a task group 7 (TG7) which specifies and registers the required standards for VLC.

Similar to other wireless optical communication systems, VLC is aimed to allow high data rate communication between users. As an example, project OMEGA was intended to deliver 100+ Megabit/second (Mbit/s) data rate via interior lighting. However, as detailed in Sec. 2.1.4, the low modulation bandwidth of the LED, namely ~ 2 megahertz (MHz) for white LEDs, restricts data rate [24]. In terms of signal to noise ratio (SNR), visible light communication systems possess high SNRs [25] . As also illustrated in Sec. 2.4, SNRs in excess of 50 dB are available for typical VLC channels. In summary, the VLC channel can be characterized as low bandwidth with very high SNR. Therefore, there are several different techniques that can be employed to achieve higher data rates.

1.1.1 Methods to improve the data rate

As stated earlier, the modulation bandwidth of the LED is limited. As an example, the modulation bandwidth of a phosphor-based white LED is limited to ~ 2 MHz. To mitigate this effect, a common method is to employ optical filtering discussed in Sec. 2.1.5. For white LEDs, for example, detecting only the blue component of the emission enhances the modulation bandwidth to ~ 20 MHz, albeit at the expense of some reduction in the received power.

Other than optical filtering, the work of [26] suggests transmitter equalization as a technique to increase VLC data rate. In that scenario, an array of LEDs with different peak frequencies are used to create a channel that has an improvement of a factor of 10 in the bandwidth. Using this method, a 2 meter (m) distance is covered

with 40 Mbit/s non-return-to zero on-off keying (NRZ OOK) and a bit error rate (BER) of less than 10^{-6}. Mixing this technique and blue filtering at the receiver, an 80 Mbit/s link with the same BER is reported for the same distance coverage.

As another alternative, orthogonal frequency division multiplexing (OFDM), detailed in Sec. 2.5.1, is suggested. Through simultaneous transmission of lower data rates on parallel subcarriers instead of a high rate serial data, it is shown that OFDM has the capability to achieve higher data rates while each subcarrier is operating within a narrow band. Using blue filtering, previous work in [27] reports 125 Mbit/s data rate over 5 m distance with NRZ OOK modulation and uncoded BER of less than 2×10^{-3}. For the same BER, data rates of more than 200 Mbit/s are achieved in [28] using OFDM.

Apart from the discussed methods, the work in [29] suggests using optical multiple input multiple output (MIMO) techniques on VLC to achieve data rates of up to several hundreds of Mbit/s.

1.1.2 VLC Challenges

Although the discussed methods enhance the communication data rates, still very high data rates (more than a Gbit/s) are unachievable even with optical filtering and equalization techniques.

Apart from the challenge of achieving higher data rates, there are additional challenges for VLC. As discussed in [30], providing a high speed VLC uplink is difficult. In [31], a reflecting transceiver is proposed. The reflector receives the incident light and returns a portion of the beam to the transmitter. However, the data rates achieved from this method are low (less than 50 Mbit/s).

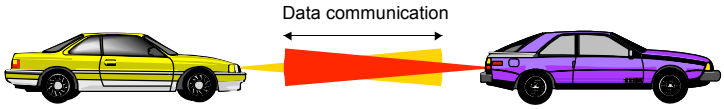

Figure 1.2: Car-to-car visible light communication between head and tail lights [36].

Another challenge for VLC is to cooperate with another wireless standard such as RF. The work in [32] examined the combination of a high speed downlink and a lower speed RF wireless LAN and showed that the combined system possess some benefits in terms of latency and throughput. Also the work in OMEGA project aims to combine different RF and optical wireless to achieve the desired performance [14].

1.2 VLC Applications

The applications of VLC are not restricted to indoor uses. Some main applications of VLC are detailed in the following.

- **Vehicle and transportation:**

  White LEDs can also be used in the automotive field to communicate audio or digital data between cars, between traffic infrastructure and cars, between robots or even between aircraft [33, 34]. The first cars that employ LEDs as headlights are now appearing [35]. Figure 1.2 displays visible light communication between head and tail lights of two cars [36].

- **Hospitals and healthcare:**

  Visible light is well-suited for communication in hospitals and healthcare, especially around MRI scanners and in operating theatres where RF radiations are

undesirable. There is an ongoing project in Japan that is intended to incorporate VLC applications to hospitals and healthcare [37].

- **Hazardous environments:**

  Visible light communications is an attractive choice for areas where there is a risk of explosions (such as mines, petro-chemical plants, oil rigs etc.) as it provides both safe illumination and communications.

- **Location based services:**

  There exist some applications for VLC that enable estimation of user location. The geospatial information authority (GSI) in Japan has already started the activity of indoor location estimation using white LEDs [38].

- **Defence and security services:**

  Visible light is a strong candidate for new defence and security systems. The fact that visible light cannot be detected on the other side of a wall has considerable security advantages.

- **Aviation:**

  Light emitting diodes are already used in aircraft for illumination and can also be employed to provide media services to passengers. Such application reduces the aircraft cost and weight since there is no need of wires [39].

- **Underwater communications:**

  Visible light is very attractive for environments where radio waves do not propagate for a long distance. Since radio waves do not travel well through thick electrical conductors like water, VLC can be used as an alternative to support

underwater communications. Such advancement can enable underwater vehicles and divers to communicate to each other. The work in [40] uses green light for underwater communications of up to 30 meter distance. Underwater visible light communication is also illustrated in [41].

The applications discussed in this section focus on the use of visible light for illumination and data communication, with illumination as the main function. However, there exist some VLC applications in which illumination is not important. The work in [42] suggests a different application of visible light for only data transmission. The experimental link proposed in this work uses visible red light lasers (650 nm red beam) for free-space optical communications to cover a range of 300 m at a potential data rate of 100 Mbit/s.

1.3 Thesis Contributions

In this thesis, efficient OFDM signaling schemes for VLC systems are proposed. As shown in Sec. 2.5.1, DC-biased OFDM, asymmetrically clipped optical OFDM (ACO-OFDM) and pulse amplitude modulated discrete multi-tone (PAM-DMT) are examples of IM/DD compatible OFDM schemes. However, as it will also be detailed in Chapter 2, they have several drawbacks. In general, DC-biased OFDM signals suffer from poor average optical efficiency [43]. Clipped multi-carrier systems such as ACO-OFDM [44, 45, 46, 47, 48] and PAM-DMT [49] provide better optical power efficiency compared to DC-biased OFDM. However, this is achieved at the expense of losing half the degrees of freedom and requiring higher PAPR compared to DC-biased OFDM. Furthermore, conventional ACO-OFDM and PAM-DMT receivers do not exploit the time domain inherent structure in detection.

In this thesis, a novel bandwidth efficient method to implement OFDM on IM/DD channels is presented and termed *spectrally factorized optical* OFDM (SFO-OFDM) [50]. The loss of half the degrees of freedom and high PAPR in ACO-OFDM and PAM-DMT are mitigated in SFO-OFDM. The proposed technique achieves gain both in average required transmitted power and PAPR compared to previous approaches.

Furthermore in this thesis, a new receiver design scheme is proposed and simulated for clipped multi-carrier systems [51]. Previous deigns for such systems do not take advantage of the structure of the time signal in detection [44, 48]. Exploiting such structure in the receiver, a new maximum likelihood (ML) detector is proposed and shown to improve the optical power efficiency of the system.

1.4 Thesis Structure

This thesis is organized as follows:

In Chapter 2, a detailed description of visible light communication channels is provided. Light emitting diodes (LEDs) and optical photodiodes are introduced as the transmitters and receivers in visible light communication systems. The amplitude constraints of IM/DD channels are then discussed and the channel model between the transmitter and the receiver is presented. For VLC channels, large signal-to-noise ratios are illustrated through an indoor VLC example. Finally, compatible OFDM schemes for IM/DD channels, such as DC-biased OFDM, ACO-OFDM and PAM-DMT, are analyzed in detail and the framework of the thesis is established.

In Chapter 3, spectrally factorized optical OFDM is developed and suggested as a method of choice for implementing OFDM on IM/DD channels. Through proving a theorem, the framework of SFO-OFDM is established and used for design schemes.

It is shown that SFO-OFDM mitigates the problem of requiring reserved subcarriers and high PAPR in ACO-OFDM and PAM-DMT. Furthermore, a noticeable gain is achieved by implementing a sub-optimal 9-subcarrier SFO-OFDM in comparison with ACO-OFDM, PAM-DMT and DC-biased OFDM.

In Chapter 4, a new pairwise maximum likelihood (ML) detector for ACO-OFDM and PAM-DMT systems is proposed. It is verified through simulation that by using the inherent structure of the time samples in ACO-OFDM and PAM-DMT, a considerable gain in optical power efficiency can be achieved.

Finally, the thesis concludes in Chapter 5 with conclusions and suggestions for future work.

Chapter 2

Visible Light Communication Channels

In order to implement efficient optical OFDM on VLC channels, it is important to model the behavior of the channel. In this chapter, the basic properties of VLC channels are introduced. The transmitter and receiver devices are discussed and the channel is modeled. An example of an indoor VLC application is illustrated and finally, current IM/DD compatible OFDM schemes are explicitly presented and the framework of the thesis is established.

2.1 Basic Channel Properties

2.1.1 IM/DD Channels

Similar to other wireless optical communication systems, VLC relies on intensity modulation and direct detection (IM/DD) for data transmission. Figure 2.1 displays a

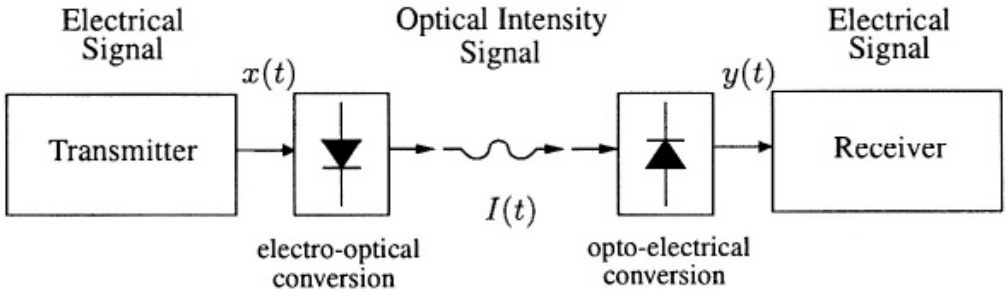

Figure 2.1: A block diagram of an intensity modulated direct detection channel [52].

block diagram of an intensity modulated direct detection system [52]. The instantaneous optical intensity, $I(t)$, is modulated proportional to the input electrical current $x(t)$. This method of modulation is termed as intensity modulation and can be done by a laser diode (LD) or a light-emitting diode (LED). Usually, LEDs have higher reliability, lower cost and are considered more eye-safe compared to laser diodes. However, the main advantage of laser diodes is their higher speed of operation [52].

After data modulation, the intensity signal is transmitted through the channel. At the receiver, a photodiode is used to detect the received intensity. This method of detection is termed as direct detection.

The basic properties of photodiodes are discussed in Sec. 2.1.2.

2.1.2 Photodiodes

Photodiodes are solid-state devices that are used to perform the optical to electrical conversion. They produce an output electrical current, $y(t)$, proportional to the received intensity signal. The received current is then processed to extract the transmitted information.

The key parameter in photodiodes is the responsivity defined as,

$$R = \frac{I_p}{P_p}, \tag{2.1}$$

where I_p is the average photocurrent generated and P_p is the incident optical power. The photodiode responsivity depends on the physical structure of the photodiode and has the units of ampere per watt ($\frac{A}{W}$). Two common photodiodes that are currently used in practice are p-i-n photodiodes and avalanche photodiodes. The first type has lower cost but lower modulation bandwidth [52].

The received power of the photodiode, P_p, is proportional to its effective light-collection area. Thus, the photodiode effective area must be large enough to collect the transmitted signal. In general, photodiodes must be selected such that the cost, performance and safety requirements are satisfied.

As stated in Chapter 1, visible light communication allows the simultaneous use of light for both illumination and data modulation. Visible light communication systems employ light emitting diodes (LEDs) as optical transmitters. In the next section, the basic physical and operational characteristics of LEDs are presented and discussed.

2.1.3 LED Characterization

A light-emitting diode (LED) is a semiconductor light source. Two important lighting factors of LEDs are color rendering index and luminous efficacy. The color rendering index is a measure of the ability of the LED to produce color in comparison with an ideal light source. The luminous efficacy on the other hand, is the measure of the efficiency with which the source produces visible light from electricity. It is equal to the ratio of luminous flux, defined in Sec. 2.2, to the total electric power consumed

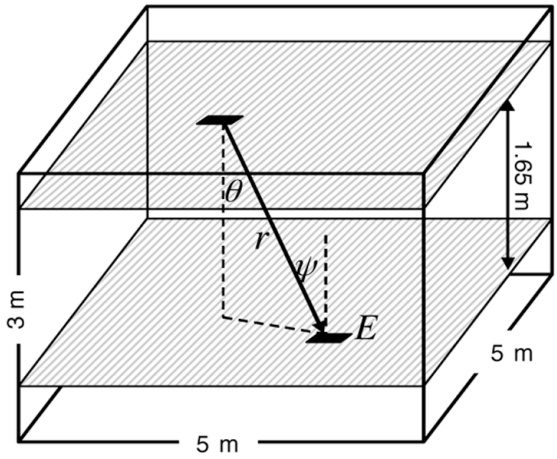

Figure 2.2: An indoor application of visible light communications [53].

by the source. Therefore it has the units of lumen per watt ($\frac{lm}{W}$).

Figure 2.2 shows a typical room with dimensions $5 \times 5 \times 3\ m^3$ where white light LEDs are set up 2.5 m above the floor, and the receiver is located at the desktop surface 0.85 m above the floor [53]. The LEDs produce white light suitable for illumination and data modulation. There are two popular methods to produce white light. These methods are introduced and discussed in Sec. 2.1.4 and 2.1.5.

2.1.4 RGB LEDs

A simple way to form white light is to mix red, green and blue (RGB) colors with appropriate portions as shown in Fig. 2.3 [54]. The LEDs produced in this way are often referred to as RGB LEDs.

Red-green-blue LEDs have the flexibility of mixing different colors and possess higher luminous efficacy (in excess of 90 $\frac{lm}{W}$ [55]) compared to phosphor-based LEDs discussed in Sec. 2.1.5. However, they are seldom used in practice to produce white

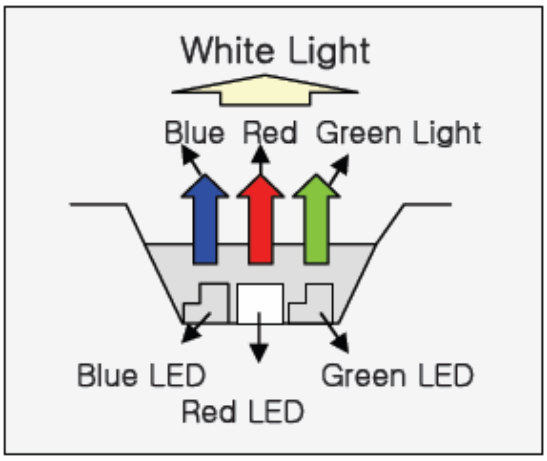

Figure 2.3: The structure of RGB white LEDs [54].

light. Other than requiring different color optical sources, RGB LEDs suffer from instability in the produced color. The RGB LED's performance degrades with rising temperature hence leads to a considerable change in the produced color [55].

2.1.5 Phosphor-based LEDs

This method involves coating a blue LED with a yellow emitting phosphor as shown in Fig. 2.4. The resulting LEDs are termed as phosphor-based white LEDs.

Phosphor-based LEDs have a lower luminous efficacy compared to RGB LEDs ($\sim$ 80 $\frac{lm}{W}$) due to phosphor-related degradation issues [55]. However, the majority of white LEDs that are currently in use on the market are manufactured using this technology. Apart from the advantage of requiring only a single color source, these types of LEDs are easier to design and are less expensive than complex RGB LEDs. Furthermore, the available modulation bandwidth of such LEDs can be enhanced by at least an order of magnitude using blue filtering. Due to the long decaying time of the phosphor, the modulation bandwidth of the white emission is limited to $\sim$ 2 MHz.

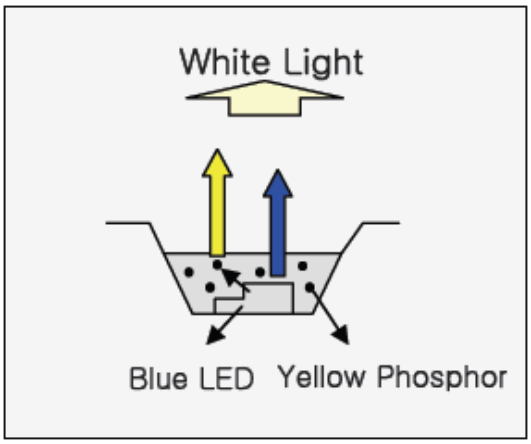

Figure 2.4: The structure of phosphor-based white LEDs [54].

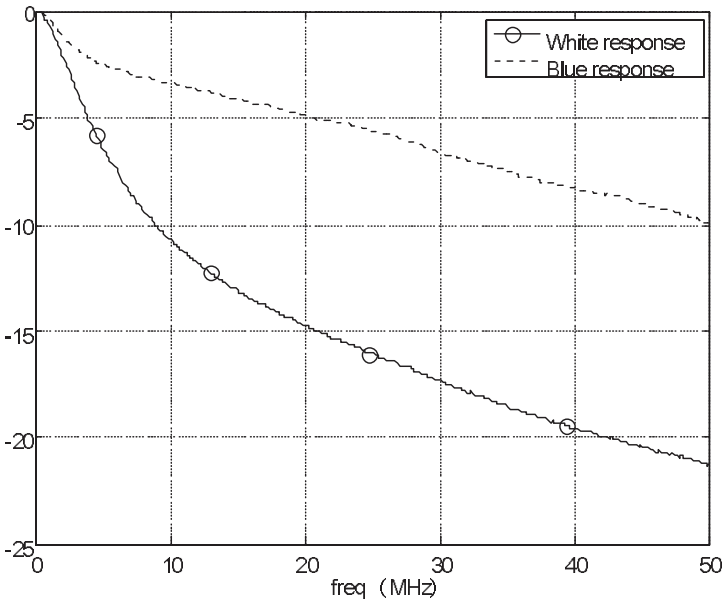

Figure 2.5: Available modulation bandwidth of an OSRAM white light LED both for white and blue component [25].

However, the blue component has a larger modulation bandwidth $\sim$ 20 MHz. As a result, to achieve a higher modulation bandwidth and therefore higher data rates, a common method is to only detect the blue part of the spectrum at the receiver termed as blue filtering. The blue filtering approach was first adopted in the recently completed project OMEGA in Europe with the aim of providing 100+ Mbit/s data rate via interior lighting [15]. The white LEDs used in project OMEGA are products of OSRAM with a modulation bandwidth as shown in Fig. 2.5 both for blue and white component [25]. A new LED concept from OSRAM, termed as "Brilliant-Mix", has been shown to achieve a high luminous efficacy [56]. These new trends provide 110 $\frac{lm}{W}$ luminous efficacy which is 30% greater than typical phosphor-based white LEDs.

Apart from OSRAM, there exist other LED producers such as Philips [57], Personik [58], NICHIA [59], VISHAY [60] and others. All the mentioned companies produce LEDs that are available in different sizes, from 3 mm to 10 mm, and different colors. Other than white, LEDs are available in various colors such as green, red, blue, royal blue, cyan, red-orange and amber.

2.2 Illumination using white LEDs

As mentioned earlier in this chapter, the primary function of visible light is illumination. Enforced by the standards, VLC is done very fast such that it is not perceptible to the eye.

In order to have appropriate lighting, a certain illuminance is required at the illuminated surface. The illuminance E, with unit lux (lx), is defined as luminous

flux Φ, with unit lumen (lm)

$$\Phi = 683 \, \frac{lm}{W} \int_{\lambda_{min}}^{\lambda_{max}} V(\lambda) P(\lambda) d\lambda, \tag{2.2}$$

per unit area [24]. In (2.2), $V(\lambda)$ is the eye sensitivity function (or luminous efficiency curve) as shown in Fig. 2.6 [61], and $P(\lambda)$ is the emission spectrum of the LED. The illuminance E will then be equal to,

$$E = \frac{d\Phi}{dA} = \frac{1}{r^2} \frac{d\Phi}{d\Omega} = \frac{I(\theta)}{r^2}, \tag{2.3}$$

in which Ω is the solid angle, $I(\theta) = \frac{d\Phi}{d\Omega}$, with units of candela (cd), is the luminous intensity in the direction θ from the source, and r is the distance to the illuminated surface as shown in Fig. 2.2 [30].

Figure 2.7 displays the emission spectrum of a LUXEON star white light LED product of OSRAM [62]. The left side corresponds to the fast response of the blue component ($\sim 380 - 500$ nm), whereas the right side is in correspondence with the slow yellow response ($\sim 500 - 720$ nm).

As can also be seen in Figs. 2.6 and 2.7, a typical human eye will respond to wavelengths from $\lambda_{min} \cong 380$ nm to $\lambda_{max} \cong 720$ nm in the visible light domain. Also, the human eye generally has its maximum sensitivity at around $\lambda = 555$ nm, in the green region of the optical spectrum.

For a source that obeys Lambert's emission law, $I(\theta) = I_0 \, \cos^m(\theta)$ and the horizontal illumination at the surface in Fig. 2.2 can be derived from,

$$E_h = E \cos(\psi) = I_0 \, \frac{\cos^m(\theta) \cos(\psi)}{r^2}, \tag{2.4}$$

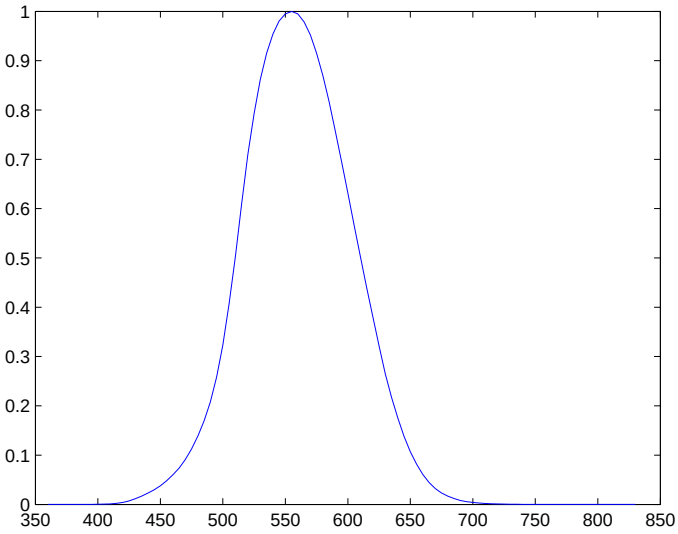

Figure 2.6: Luminous efficiency curve showing sensitivity of human eye to different wavelengths [61].

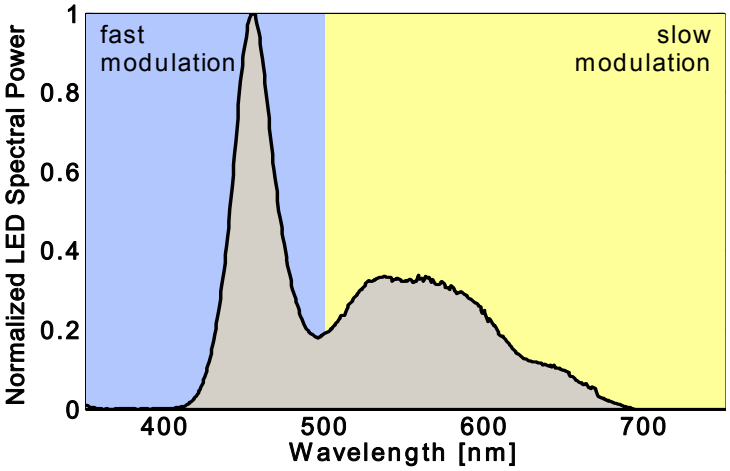

Figure 2.7: Emission spectrum of a LUXEON star white light LED [62].

where $I_0 = I(\theta = 0)$ is the maximum luminous intensity, m is the Lambert index, and ψ is the angle of incidence. The Lambert index depends on the semi-angle at half illuminance, $\theta_{1/2}$, as:

$$m = -\frac{1}{\log_2 \theta_{1/2}}. \tag{2.5}$$

The illuminance of the light is governed by International Organization for Standardization (ISO) [63]. In accordance with this standard, for an indoor communication model such as the one in Fig. 2.2, the minimum required average illuminance suitable for writing, reading and typing is 400 lx at the desktop height. Moreover, the illuminance between $200 \sim 800$ lx is required throughout the room span.

The source optical power is defined as the average radiation spectrum,

$$P = \int_{\lambda_{min}}^{\lambda_{max}} P(\lambda)\ d\lambda. \tag{2.6}$$

By having $P(\lambda)$ and $V(\lambda)$, one can find P and Φ. For LUXEON star LEDs, the conversion factor of $\alpha = \frac{P}{\Phi} = 2.1$ mW/lm is found between the source optical power in the blue region and the luminous flux.

2.3 Channel Modeling

In visible light communications, similar to other IM/DD systems, the channel model can be expressed as:

$$y_r(t) = R\ x(t) * h(t) + w(t), \tag{2.7}$$

where $y_r(t)$ is the received signal current $[A]$, $x(t)$ is the transmitted intensity signal $[W]$, $h(t)$ is the VLC channel impulse response, $w(t)$ is the VLC channel noise $[A]$, R is the detector responsivity $[\frac{A}{W}]$, and $*$ denotes convolution [43]. If the channel impulse response in known at the receiver, a zero forcing equalizer (ZFE), $c(t)$, such that

$$R\ c(t) * h(t) = \delta(t), \tag{2.8}$$

can be used to make the channel flat

$$y(t) = x(t) + z(t), \tag{2.9}$$

where $y(t) = c(t) * y_r(t)$ is the equalized received signal and $z(t) = c(t) * w(t)$ is the equalized noise.

Notice that data are modulated on the instantaneous intensity of the LEDs. Hence,

$$x(t) \geq 0. \tag{2.10}$$

Due to eye-safety regulations governed by International Electrotechnical Commission (IEC)[64], the average intensity of all emissions is also bounded:

$$P_{ave} = \lim_{T\to\infty} \frac{1}{2T} \int_{-T}^{T} x(t)\ dt \leq P_0. \tag{2.11}$$

Furthermore, optical sources have limited dynamic linear range due to their nonlinear behaviour [65]. The dependence of the output optical power of the LEDs to the driving current of the LEDs is nonlinear and distorts the transmitted signal. The distortion is more considerable at higher optical powers. Therefore, it is always desired that

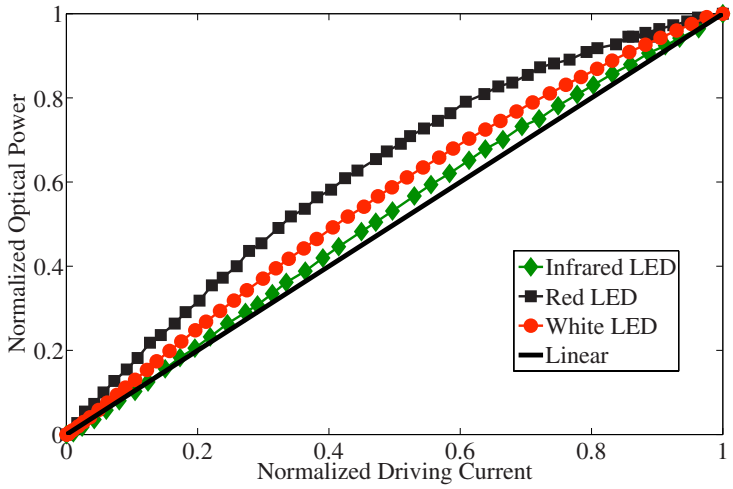

Figure 2.8: Nonlinear behaviour of several different LED types [66].

the peak of the signal is not larger than a certain value, A, which leads to a peak amplitude constraint as,

$$x(t) \leq A. \tag{2.12}$$

The peak-to-average power ratio (PAPR) is then defined as,

$$\text{PAPR} = \frac{x(t)_{\max}}{P_{ave}}. \tag{2.13}$$

Figure 2.8 displays the nonlinearity behaviour of a white LED (NICHIA NSPW500Cs), red LED (NICHIA NCSR119), and infrared LED (VISHAY TSSF5210) [66]. For simplicity, the non-linearity effect is not considered in this thesis and it is assumed that predistortion techniques are employed to cancel non-linearity effects.

As stated earlier, the main properties of channels are channel impulse response and channel noise. The VLC channel impulse response and VLC channel noise are discussed in Sec. 2.3.1 and Sec. 2.3.2 respectively.

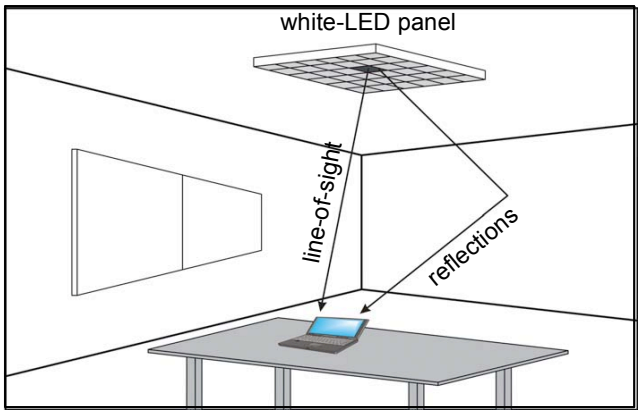

Figure 2.9: This figure displays indoor VLC between an array of white LEDs as the transmitter and a laptop as the receiver [36].

2.3.1 Channel Impulse Response

Figure 2.9 shows a typical indoor VLC channel between an array of white LEDs as the transmitter, and a laptop as the receiver. Like other wireless optical channels, the VLC channel $h(t)$ consists of a line-of-sight (LOS) component and a diffuse or non-line-of-sight component (NLOS) [24]:

$$h(t) = h_{LOS}(t) + h_{DIFF}(t). \tag{2.14}$$

The LOS contribution is the amount of signal received at the receiver directly from the transmitter and can be modeled by delayed Dirac pulses as,

$$h_{LOS}(t) = \eta_{LOS}\ \delta(t - \Delta t_{LOS}), \tag{2.15}$$

where η_{LOS} and Δt_{LOS} are the gain and the delay of the LOS signal.

The diffuse portion, however, comes from the reflections off the walls or other

objects present in the environment. This part consists of long lasting decay and can be modeled by a decaying exponential function in time domain or as follows in frequency domain [67],

$$H_{DIFF}(f) = \eta_{DIFF} \ \frac{\exp\left(-j2\pi f \Delta t_{DIFF}\right)}{1 + jf/f_0}. \tag{2.16}$$

In (2.16), η_{DIFF} and Δt_{DIFF} are the gain and the delay of the diffuse portion, and f_0 is the 3-dB cut-off frequency of a purely diffuse channel. The channel response in frequency domain can then be summarized as:

$$H(f) = \eta_{LOS} \ \exp\left(-j2\pi f \Delta t_{LOS}\right) + \eta_{DIFF} \ \frac{\exp\left(-j2\pi f \Delta t_{DIFF}\right)}{1 + jf/f_0}. \tag{2.17}$$

Therefore, the VLC channel DC gain, $H(0)$, is equal to:

$$H(0) = \eta_{LOS} + \eta_{DIFF}. \tag{2.18}$$

The LOS and diffuse gains in VLC channels can be obtained from [53] as,

$$\begin{aligned} \eta_{LOS} &= A_R(m+1) \ \frac{\cos^m(\theta_0)\cos(\psi_0)}{2\pi r_0^2}, \\ \eta_{DIFF} &= \frac{A_R}{A_{ROOM}} \frac{\rho}{1-\rho}, \end{aligned} \tag{2.19}$$

where A_R is the effective receiver area, A_{ROOM} is the room area, and ρ is the average reflectivity from the walls. As also displayed in Fig. 2.2, θ_0 and ψ_0 are the angles of irradiance and incidence, and r_0 is the distance between the receiver and the LED. Usually, the LOS contribution considerably dominates the channel response in most

scenarios [24]. Therefore, in Sec. 2.4 where an indoor VLC example is illustrated, only LOS contribution of the VLC channel is considered.

2.3.2 Channel Noise and SNR

In most wireless optical communication systems, there exist background noise originating from ambient light in the environment. Ambient light can arise from sunlight, skylight, incandescent and fluorescent lamps, or other light sources [68]. Figure 2.10 shows the normalized optical power spectra of some common background noise sources versus wavelength [43]. The background noise present in the environment leads to a DC photocurrent that causes a shot noise at the receiver. This noise source is signal independent and is the result of summation of many independent Poisson distributed random variables. Hence, it can be modeled as a Gaussian distribution [52].

Apart from shot noise, there also exists thermal noise coming from the receiver electronics. Thermal noise is also generated independent of the received signal and can be modeled as an additive white Gaussian process [52]. The total noise can then be modeled as an additive white Gaussian process with a total variance σ^2 coming from shot noise and thermal noise [43, 69]. Since the shot noise and thermal noise are uncorrelated, then:

$$\sigma^2 = \sigma^2_{shot} + \sigma^2_{thermal}. \tag{2.20}$$

It is shown in [13] that the shot noise is the dominant noise source in VLC channels. The noise power is therefore equal to:

$$\sigma^2 \cong N_{shot} B = qIB, \tag{2.21}$$

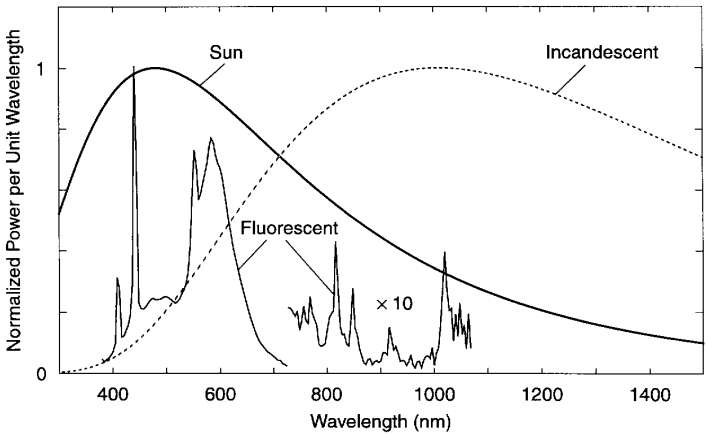

Figure 2.10: Optical power spectra of some common background noise sources versus wavelength [43].

where $N_{shot} = qI$ is the power spectral density of the shot noise, I is the induced current in the photodiode coming from ambient light, $q = 1.6 \times 10^{-19}$ is the electron charge, and B is the effective noise bandwidth. The optical and electrical SNR can then be defined as follows respectively,

$$SNR_o = \frac{P_r}{\sigma}, \tag{2.22}$$

$$SNR_e = \frac{R^2 \ P_r^2}{\sigma^2}, \tag{2.23}$$

where:

$$P_r = H(0) \ P_{ave}, \tag{2.24}$$

is the received optical signal power, $H(0)$ is the VLC channel DC gain defined in (2.18), and P_{ave} is the average transmitted power defined in (2.11).

As stated in Sec. 2.3, peak of the signal imposes notable design restrictions. Therefore, another important parameter in IM/DD channels is optical peak signal-to-noise ratio (PSNR) defined as,

$$\text{PSNR} = \frac{x(t)_{\max}}{\sigma}. \tag{2.25}$$

2.4 An Indoor VLC Example

An example of indoor data transmission via white LEDs is illustrated in [53]. In order to limit the number of LEDs for illumination, the LUXEON star LEDs with large radiation angle are chosen. The output optical power of the LEDs can be calculated using $\alpha = 2.1\ mW/lm$ conversion factor discussed in Sec. 2.2. Two scenarios shown in Fig. 2.11 are assumed for LEDs positioning. The number of LEDs and the space between them in each scenario are assumed such that the standard required brightness discussed in Sec. 2.2 is provided throughout the room. In the first scenario, A, the ceiling is covered uniformly with 16-cm-spaced white LEDs whereas in the second scenario, B, four 1 m^2 square surfaces are covered with 7-cm-spaced white LEDs. Figure 2.12 displays the optical characteristics of each LED along with measured statistics of the experiment. As can be seen, the number of LEDs used in both scenarios is less than 1000. Also in both scenarios, the major portion of the room has the minimum required brightness.

As stated in [53], the noise power is dominated by shot noise coming from ambient light. The ambient light in the area of the experiment produced $I = 0.62\ mA$ current in the receiver photodiode after blue filtering. The noise power spectral density is

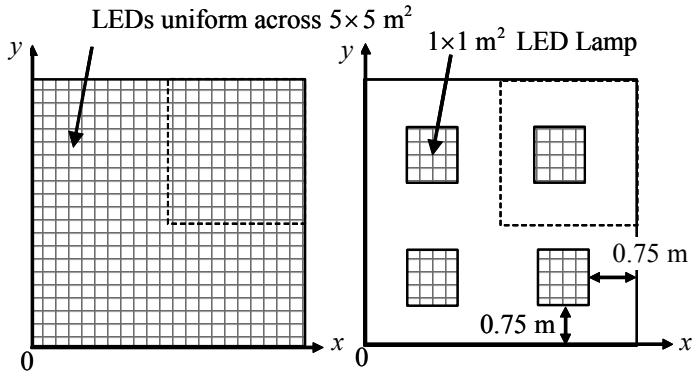

Figure 2.11: The ceiling LED designs in two different scenarios for an indoor VLC example [53].

Parameter	Scenario A	Scenario B
LED characteristics		
$2\theta(m)$	120° (1)	
I_0	9.5 cd	
P_T	63 mW	
Scenario characteristics		
LED distribution across the ceiling	uniform	4 lamps
LED chip spacing	16 cm	7 cm
Number of chips	961	784
Brightness statistics		
E (min, max)	(237,855) lx	(181,855) lx
$E \geq 400$ lx	89.7 %	80.2 %
Transmission statistics		
max LOS delay	5.5 ns	
Channel min f_{3dB}	>200 MHz	98 MHz
P_R (min, av, max)	(0.1, 0.4, 0.5) mW	
SNR (min, max)	(49, 60) dB	(47, 60) dB
$SNR \geq 54.5$ dB	88%	79%

Figure 2.12: This figure shows the optical characteristics of the LUXEON star white LEDs used in this example along with the scenario characteristics and measured statistics of the experiment [53].

then equal to:

$$N_0 \cong N_{shot} = qI = 10^{-22}, \tag{2.26}$$

Thus the noise power in (2.20) will be,

$$\sigma^2 \cong \sigma^2_{shot} = N_0 B = 2 \times 10^{-15}, \tag{2.27}$$

where $B = 20$ MHz is the available modulation bandwidth of the LED after blue filtering. The total received power at the receiver P_r, and the total illuminance at the surface are equal to sum of the received powers and illuminances from the LEDs. However, as stated in Sec. 2.3.1, the LOS contribution greatly dominates the channel frequency response. For the LOS part, using (2.18) and (2.24):

$$\begin{aligned} P_r &= \sum_{i=1}^{N_{LED}} H_i(0) P_{ave}, \\ H_i(0) &= \eta_{LOS,i}, \end{aligned} \tag{2.28}$$

where N_{LED} is the total number of the LEDs for each scenario. Considering $P_{ave} = P_{CHIP}$ for each LED, and replacing (2.19) in (2.28) gives:

$$\begin{aligned} P_r &= P_{CHIP} \sum_{i=1}^{N_{LED}} \eta_{LOS,i} \\ &= P_{CHIP}\ A_R\ (m+1) \sum_{i=1}^{N_{LED}} \frac{cos^m(\theta_i) cos(\psi_i)}{r_i^2}. \end{aligned} \tag{2.29}$$

Also from (2.4),

$$E_h \;=\; \sum_{i=1}^{N_{LED}} E_{h_i} = I_0 \sum_{i=1}^{N_{LED}} \frac{cos^m(\theta_i)cos(\psi_i)}{r_i^2}. \tag{2.30}$$

Thus the following relation exists between P_r and E_h:

$$P_r = \frac{P_{CHIP}\ (m+1)}{I_0}\ A_R\ E_h = \beta\ A_R\ E_h. \tag{2.31}$$

Therefore, the electrical SNR in (2.22) can be found from,

$$SNR_o = \frac{(R\ E_h\ A_R\ \beta)^2}{N_0 B}. \tag{2.32}$$

For this experiment, photodetectors with responsivity of $R = 0.28\ \frac{A}{W}$, and effective area of $A_R = 3\ cm^2$ are used at the receiver. Also the Lambert index is:

$$m = -\frac{1}{log_2(cos(\frac{\pi}{3}))} = 1. \tag{2.33}$$

Replacing $I_0 = 9.5$ cd and $P_{CHIP} = 63\ mW$ for the LUXEON star LEDs from Fig. 2.12, $m = 1$, $R = 0.28\ \frac{A}{W}$, $A_R = 3\ cm^2$, $E_h = 400$ lx as the required brightness, and $N_0 B = 2 \times 10^{-15}$ from (2.27), leads to $SNR_o = 54.5$ dB at the 400 lx illuminated surface. Figure 2.13 displays the received electrical SNR distribution under the areas within dashed lines in Fig. 2.11.

In summary, VLC channels have low bandwidth, restricted by the modulation bandwidth of LEDs, but high SNRs often in excess of 50 dB. Compatible VLC signaling schemes are discussed in the next section.

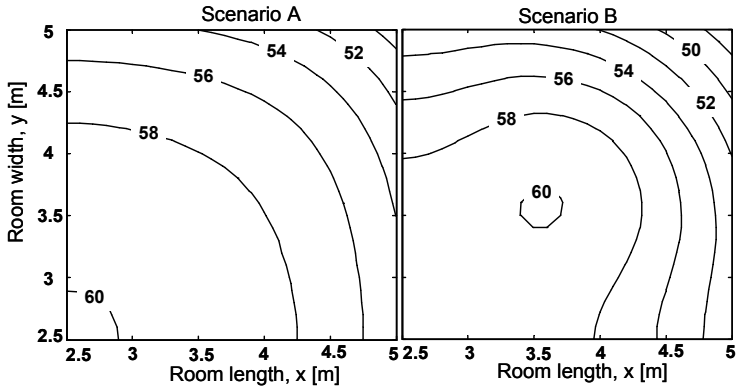

Figure 2.13: Distribution of electrical SNR [dB] under the dashed area in the room of Fig. 2.11 for both scenarios [53].

2.5 Compatible VLC signalling schemes

As discussed earlier in this Chapter, the modulated electrical amplitudes must satisfy the non-negativity constraint of IM/DD channels. This constraint does not permit direct application of conventional electrical modulations on IM/DD channels. Various compatible modulation techniques for such channels include on-off keying (OOK) modulation, pulse-position modulation (PPM), and subcarrier modulation (SM).

The simplest modulation technique is binary on-off keying which represents data as the presence or absence of a signal. In its simplest form, the presence of a pulse for a specific time duration, $T = 1/R$ (R is the bit rate), denotes a binary one, whereas its absence for the same duration time denotes a binary zero. This type of modulation is usually referred to as non-return-to-zero on-off keying (NRZ OOK) and is displayed in Fig. 2.14, with P denoting the average transmitted power. In general, OOK signals suffer from low average optical power efficiency [43].

Pulse-position modulation (PPM) is a modulation method in which information is modulated on the position of the pulses. Pulse-position modulation (PPM) of average

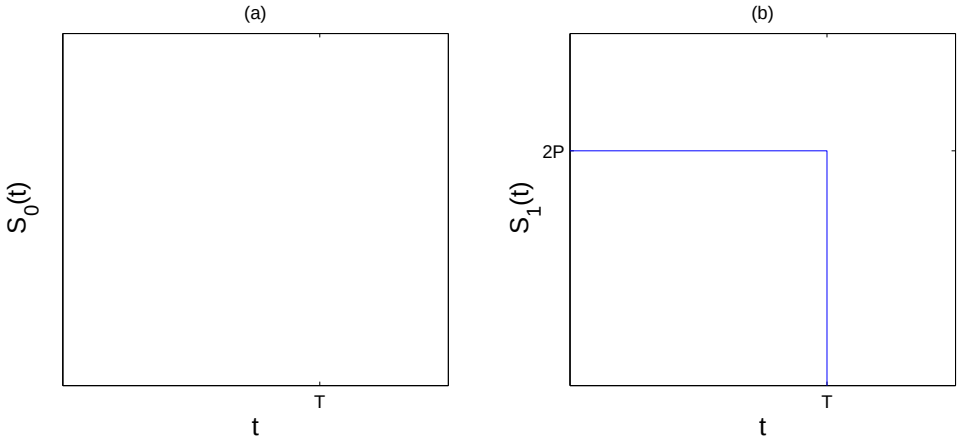

Figure 2.14: NRZ OOK modulation technique: (a) denoting binary zero, and (b) denoting binary one.

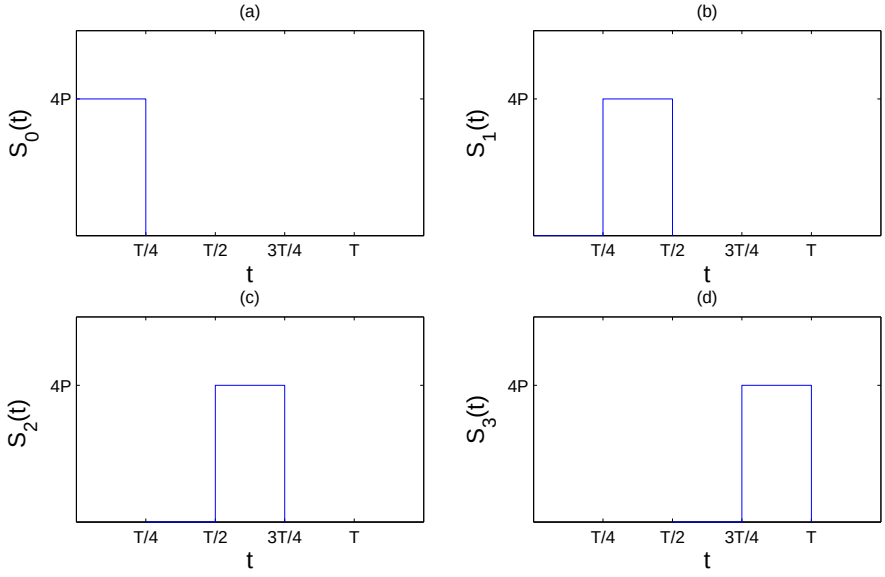

Figure 2.15: 4-PPM transmitted waveforms: (a) denotes 00, (b) denotes 01, (c) denotes 10, and (d) denotes 11.

power P consists of L time slots (or chips) denoting $\log_2 L$ bits in which a constant power of LP is transmitted during one of the chips and zero power is transmitted during other chips. Because of its higher peak optical power, the use of L-PPM decreases the required transmitted power to achieve a desired BER compared to OOK, however, it also increases the required receiver bandwidth by a factor of $L/\log_2 L$ for a given bit rate. Figure 2.15 displays the 4-PPM transmitted waveforms.

Subcarrier modulation is a modulation scheme where information is modulated onto a number of sinusoidal waveforms termed as subcarriers. In its simplest form, data are modulated onto a single subcarrier located at a certain frequency $f_0 = 1/T$. This type of modulation is termed as single subcarrier modulation (SSM). Since a sinusoidal waveform takes both negative and positive amplitudes, a DC bias is required to satisfy amplitude non-negativity constraint of optical channels. Figure 2.16 displays quadrature phase-shift keying (QPSK) SSM waveforms.

Multiple-subcarrier modulation (MSM) is a subcarrier modulation scheme where information is modulated onto N orthogonal subcarriers located at different frequencies, f_k ($k = 0, 1, \cdots, N-1$). Independent bit streams are modulated onto orthogonal subcarriers while maintaining total data rates similar to conventional SSM schemes in the same bandwidth. The sum of the modulated subcarriers is modulated onto the instantaneous power of the transmitter. Similar to SSM, a DC bias is required to satisfy amplitude non-negativity constraint unless the non-negativity is already guaranteed by careful choice of subcarrier amplitudes.

Multiple-subcarrier modulation is well-suited for simultaneous transmission of data from a single base station to several receivers. Due to the orthogonality of the subcarriers, it also allows individual receivers to access only a subset of the whole

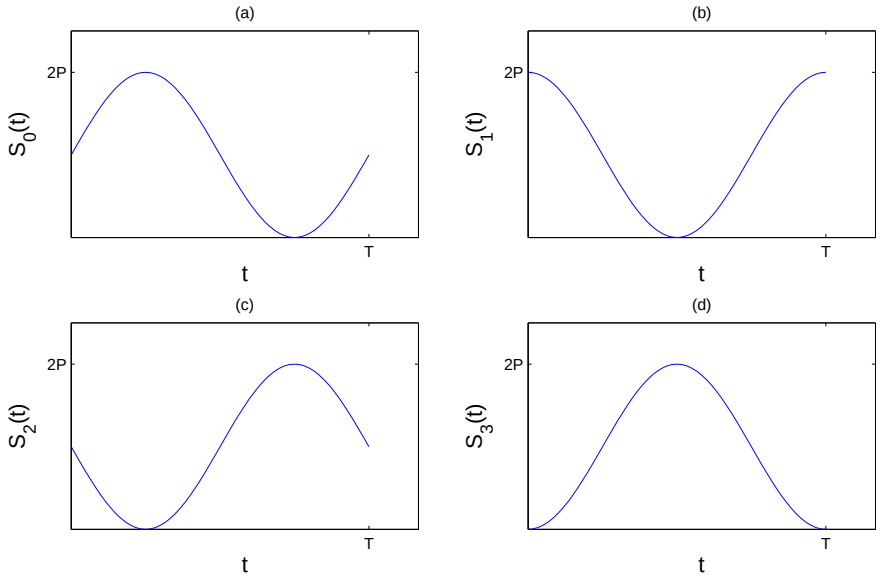

Figure 2.16: SSM for a QPSK: (a) denotes 00, (b) denotes 01, (c) denotes 10, and (d) denotes 11.

transmission. Furthermore, by simultaneous transmission of several narrowband subcarriers, MSM can achieve high aggregate bit rates while each subcarrier is operating within a narrowband.

Inter-symbol interference (ISI)

Inter-symbol interference (ISI) is a distortion in the received signal in which one symbol interferes with subsequent symbols. Usually, ISI arises in situations in which a signal from a transmitter reaches the receiver from several independent paths. This effect is known as multi-path propagation and can be caused from reflections off the walls. Since different paths have different lengths, this results in different versions of the same signal arriving at the receiver at different times, i.e. some part of the symbol will be spread into subsequent symbols hence distorting it.

Apart from multi-path propagation, another cause of ISI is the signal transmission through a frequency selective band-limited channel. Passing the signal from such channels attenuates the amplitude of the signal below the cut-off frequency. Moreover, it leads to removal of frequencies above the cut-off frequency. Such filtering not only changes the shape of the signal within the symbol period, but also will spread the symbol into subsequent symbols.

A major advantage of MSM scheme over other discussed techniques is its ability to overcome ISI by means of employing guard intervals between successive symbols. Using MSM, the channel can be viewed as using many lower symbol rates narrowband signals rather than one rapidly modulated wide-band SSM signal. Since the duration of each symbol is longer in lower symbol rate modulation schemes, it is beneficial to transmit a number of low-rate parallel streams rather than a single high rate stream. The low symbol rate of each subcarrier, allows the insertion of affordable guard intervals hence eliminating ISI.

As a special case of MSM, orthogonal frequency division multiplexing (OFDM) is proposed in which an additional advantage lies in its efficient implementation using Fast Fourier Transform (FFT).

2.5.1 Orthogonal Frequency Division Multiplexing

Orthogonal frequency division multiplexing (OFDM) is an attractive multiple subcarrier modulation scheme which has widely been employed both in wireless and cable digital communications. Other than the capability to remove ISI, the other advantages of OFDM include the ability to easily adapt to different channels and the ability to remove narrowband interference.

Some cable applications of OFDM include asymmetric digital subcarrier line (ADSL), very-high-bitrate digital subcarrier line (VDSL), power line communication (PLC), and multimedia over coax alliance (MoCA) home networking. Some notable OFDM wireless applications involve wireless local area network (WLAN) radio interfaces (IEEE 8.2.11a, g, n), the terrestrial digital TV systems, the terrestrial mobile TV systems, and the wireless personal area network (PAN) ultra wide-band (IEEE 802.15.3a).

Figure 2.17 displays the block diagram of an optical wireless communication system using OFDM. First a higher rate serial data is partitioned into N parallel data streams with lower rates. Each data stream is then mapped on a complex value using quadrature amplitude modulation (QAM) or phase-shift keying (PSK) modulation assigned with Hermitian symmetry for reality of the time signal. These complex values are then mapped onto a data vector $\mathbf{X}$:

$$\begin{aligned} N\ even: \mathbf{X} &= [X(0)\ \underbrace{X(1)\ \cdots\ X\left(\frac{N}{2}-1\right)}_{data\ values}\ 0\ \underbrace{X^*\left(\frac{N}{2}-1\right)\ \cdots\ X^*(1)}_{Hermitian\ symmetry}]^T, \\ N\ odd: \mathbf{X} &= [X(0)\ \underbrace{X(1)\ \cdots\ X\left(\frac{N-1}{2}\right)}_{data\ values}\ \underbrace{X^*\left(\frac{N-1}{2}\right)\ \cdots\ X^*(1)}_{Hermitian\ symmetry}]^T, \end{aligned} \quad (2.34)$$

where $X(0) = P$ is the required DC bias to guarantee non-negativity of time samples. For the case N even, it is assumed that no data is modulated on the middle subcarrier, i.e. $X(\frac{N}{2}) = 0$.

Performing an N-point Inverse Fast Fourier Transform (IFFT) on $\mathbf{X}$ produces real

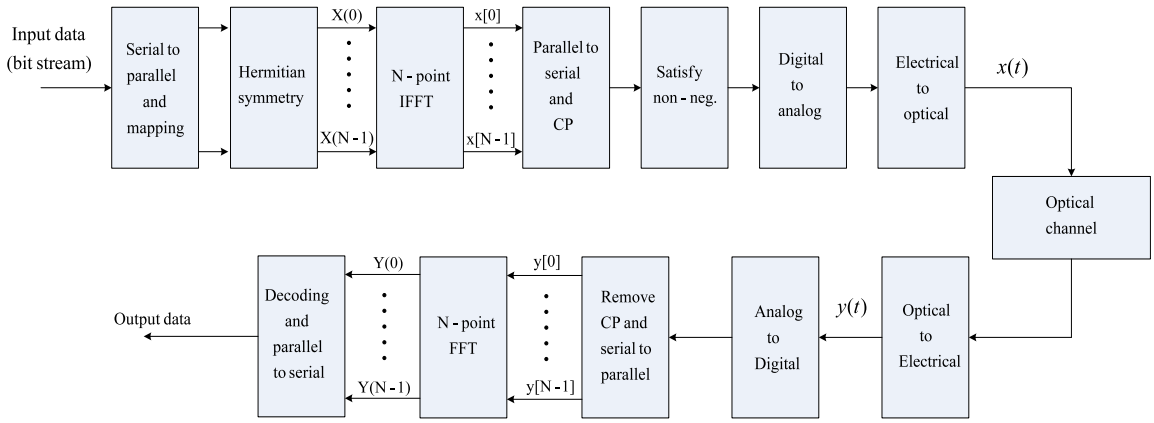

Figure 2.17: Block diagram of an optical wireless system using OFDM.

time samples $x[n]$ as,

$$x[n] = \frac{1}{N}\sum_{k=0}^{N-1} X(k)\exp\left(\frac{j2\pi nk}{N}\right) \;;\; n = 0, 1, \cdots, N-1. \tag{2.35}$$

The resulting time values are then converted back to serial. Moreover, a cyclic prefix (CP), which consists of the end of the OFDM signal, is transmitted during the guard interval to allow linear convolution of the channel be modeled as circular convolution. However, the time samples are not still appropriate for transmission through the channel and the non-negativity of them must be satisfied. This is done in the block referred to as "Satisfy non-negativity" in Fig. 2.17. Usually a DC bias is added to the time samples. This technique is termed as DC-biased optical OFDM and is explicitly detailed in Sec. 2.6.1. Previous OFDM applications on IM/DD channels, in particular VLC channels, rely on this technique to ensure non-negativity [53, 43, 24, 28, 70, 71, 72, 73, 74, 75]. As an alternative to DC-biased OFDM, asymmetrically clipped optical OFDM (ACO-OFDM), detailed in Sec. 2.6.2, and

pulse amplitude modulated discrete multi-tone (PAM-DMT), detailed in Sec. 2.6.3, are proposed. These techniques remove the requirement of a DC-bias ($P = 0$) by choosing the subcarrier amplitudes with a given structure [44, 45, 46, 49]. In such systems, anti-symmetric time samples are generated in time domain by imposing certain restrictions on subcarrier amplitudes. Hence the "Satisfy non-negativity" block simply clips the negative amplitudes at zero level to guarantee non-negativity. Notice that clipping only guarantees sample non-negativity and not the continuous signal.

After satisfying the non-negativity constraint in optical OFDM systems, the time samples are passed through a digital to analog filter and converted to an optical signal, $x(t)$, using an LED. The resulting optical signal is then transmitted through the optical channel.

At the receiver, the demodulation and decoding the data will be performed. The orthogonality of the subcarriers enables the receiver to separate each carrier and perform standard QAM or PSK maximum likelihood (ML) detection. The detected data are then compared with the transmitted data and the bit error rate (BER) as an evaluating metric for analyzing error performance of the system is found.

2.6 Compatible OFDM schemes for IM/DD channels

As discussed earlier in this chapter, the amplitude non-negativity constraint of VLC channels does not allow direct implementation of OFDM on such channels. Several techniques have been proposed to ensure the non-negativity of the OFDM signal

such as : DC-biased OFDM (DCB-OFDM), Asymmetrically Clipped Optical OFDM (ACO-OFDM), and Pulse Amplitude Modulated Discrete Multi-tone (PAM DMT). These methods and their properties are explicitly presented in the following.

2.6.1 DC-biased OFDM

As discussed in Chapter 1, OFDM signals are in general bipolar signals and have both negative and positive amplitudes. One common method that can be used to guarantee non-negativity of the transmitted signal, is to add a DC bias to the bipolar OFDM signal as in [70, 75, 76, 77, 78, 79, 80, 81, 82, 83]. The required DC bias to satisfy non-negativity is equal to the maximum negative amplitude of the OFDM signal.

For very large numbers of subcarriers, the amplitude of the OFDM signal can be approximated by a zero mean Gaussian distribution through the law of large numbers [84]. For the zero mean Gaussian distributed random variable x with standard deviation of σ, the probability of the random variable being in the region of $-2\sigma < x < 2\sigma$ is equal to 95.6 %. As a result,

$$Pr\{x + 2\sigma \ > 0\} \cong 97.8\%, \tag{2.36}$$

which is very close to 1. Therefore, another method that has been employed in recent work [45], suggests adding a DC bias equal to twice the standard deviation of the bipolar OFDM signal and clipping the resulting amplitudes at the zero level. This method requires less DC bias, however, it suffers from the distortion caused from the clipping noise.

The right diagram in Fig. 2.18 depicts the transmitted DC-biased OFDM signal

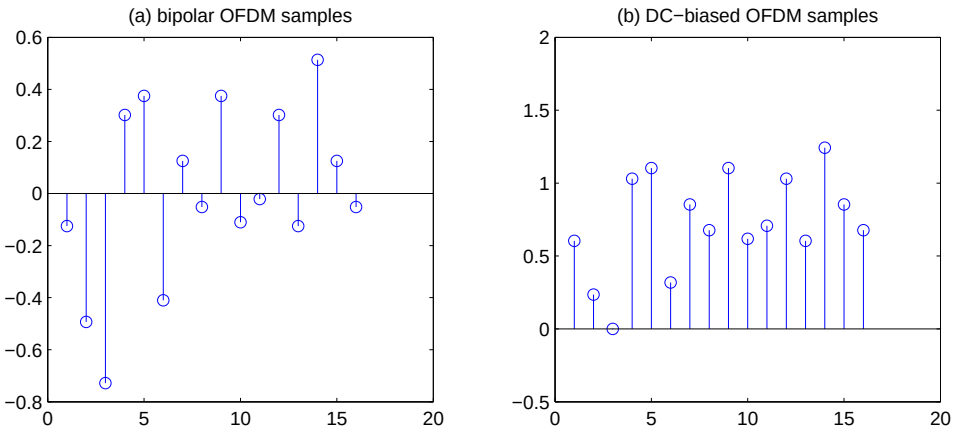

Figure 2.18: Fig. (a) shows bipolar OFDM time samples, Fig. (b) shows the DC-biased OFDM samples generated after adding a DC-bias to the bipolar samples in (a).

for a particular bit stream using $N = 16$ total subcarriers. Using (2.34) for N even, the DC subcarrier is adjusted equal to the maximum negative amplitude of the bipolar OFDM signal and the middle subcarrier is set to zero. The other subcarrier amplitudes are chosen from 4-QAM constellation points assigned with Hermitian symmetry to have a real output signal.

Although DC-biased OFDM is the simplest compatible OFDM scheme for IM/DD channels, it suffers from poor average optical power efficiency. In order to improve the optical power efficiency, clipped multicarrier systems such as ACO-OFDM and PAM-DMT are proposed. These methods are discussed in Sec. 2.6.2 and Sec. 2.6.3 respectively.

2.6.2 Asymmetrically Clipped Optical OFDM (ACO-OFDM)

In ACO-OFDM, unlike DC-biased OFDM, a constraint is imposed on the subcarrier amplitudes [44, 45, 46, 47]. Assume N to be the number of total subcarriers and

$X(k)$ be the complex value of the kth subcarrier assigned with Hermitian symmetry. Consider the case where only odd subcarriers are modulated and the even subcarriers are set to zero:

$$X(k) = 0 \ ; \ k : even. \tag{2.37}$$

From (2.35), the nth time domain sample, $x[n]$, can be found by performing IFFT on the subcarriers. Let the portion of $x[n]$ due to the kth subcarrier be denoted by $x(k, n)$ as,

$$x[k, n] \ = \ \frac{1}{N} X(k) \exp\left(\frac{j2\pi kn}{N}\right). \tag{2.38}$$

Thus:

$$x[n] \ = \ \sum_{k=0}^{N-1} x[k, n]. \tag{2.39}$$

Forming $x\left[k, n + \frac{N}{2}\right]$,

$$\begin{aligned} x\left[k, n + \frac{N}{2}\right] \ &= \ \frac{1}{N} X(k) \exp\left(\frac{j2\pi k(n + \frac{N}{2})}{N}\right) \\ &= \ \frac{1}{N} X(k) \exp\left(\frac{j2\pi kn}{N}\right) \exp(j2\pi k) = x[k, n](-1)^k. \end{aligned} \tag{2.40}$$

It can be seen in (2.40) that for k odd, $x[k, n + \frac{N}{2}] = -x[k, n]$ which results in,

$$x\left[n + \frac{N}{2}\right] = -x[n] \ ; \ n = 0, 1, \cdots, \frac{N}{2} - 1. \tag{2.41}$$

This anti-symmetry in time domain leads to the conclusion that clipping the resulting amplitudes at zero level guarantees no loss of information as the data can be recovered from the corresponding positive samples.

Consider the case of the clipped signal, $x_c[n]$, as:

$$x_c[n] = \begin{cases} x[n] & \text{if } x[n] \geq 0 \\ 0 & \text{if } x[n] < 0. \end{cases} \tag{2.42}$$

The value of the kth subcarrier, $X_c(k)$, can be found by doing an FFT on the clipped time values,

$$\begin{aligned} X_c(k) &= \sum_{n=0}^{N-1} x_c[n] \ \exp\left(-\frac{j2\pi kn}{N}\right) \\ &= \sum_{\substack{n=0 \\ x[n]\geq 0}}^{N-1} x[n] \ \exp\left(-\frac{j2\pi kn}{N}\right). \end{aligned} \tag{2.43}$$

Also, the value $X(k)$ from the unclipped signal can be found from,

$$\begin{aligned} X(k) &= \sum_{n=0}^{N-1} x[n] \ \exp\left(-\frac{j2\pi kn}{N}\right) \\ &= \underbrace{\sum_{\substack{n=0 \\ x[n]\geq 0}}^{N-1} x[n] \ \exp\left(-\frac{j2\pi kn}{N}\right)}_{X_c(k)} + \sum_{\substack{n=0 \\ x[n]<0}}^{N-1} x[n] \ \exp\left(-\frac{j2\pi kn}{N}\right). \end{aligned} \tag{2.44}$$

Notice that the first term in (2.44) is equal to $X_c(k)$. Rearranging,

$$X_c(k) = X(k) + \underbrace{\sum_{\substack{n=0 \\ x[n]<0}}^{N-1} -x[n] \exp\left(-\frac{j2\pi kn}{N}\right)}_{X_c^n(k)}. \tag{2.45}$$

The term $X_c^n(k)$ in (2.45) is the clipping noise and can be written as,

$$\begin{aligned} X_c^n(k) &= -\sum_{\substack{n=0 \\ x[n]<0}}^{\frac{N}{2}-1} x[n] \exp\left(-\frac{j2\pi kn}{N}\right) \\ &\quad - \sum_{\substack{n=\frac{N}{2} \\ x[n]<0}}^{N-1} x[n] \exp\left(-\frac{j2\pi kn}{N}\right). \end{aligned} \tag{2.46}$$

Replacing the ACO-OFDM requirement, $x[n] = -x[n+\frac{N}{2}]$, in the first term of $X_c^n(k)$ and changing the variable in its second term gives:

$$\begin{aligned} X_c^n(k) &= \sum_{\substack{n=0 \\ x[n+\frac{N}{2}]\geq 0}}^{\frac{N}{2}-1} x[n+\frac{N}{2}] \exp\left(-\frac{j2\pi kn}{N}\right) \\ &\quad - \sum_{\substack{n=0 \\ x[n+\frac{N}{2}]<0}}^{\frac{N}{2}-1} x[n+\frac{N}{2}] \exp\left(-\frac{j2\pi k(n+\frac{N}{2})}{N}\right) \\ &= \sum_{\substack{n=0 \\ x[n+\frac{N}{2}]\geq 0}}^{\frac{N}{2}-1} x[n+\frac{N}{2}] \exp\left(-\frac{j2\pi kn}{N}\right) \\ &\quad - \sum_{\substack{n=0 \\ x[n+\frac{N}{2}]<0}}^{\frac{N}{2}-1} x[n+\frac{N}{2}] \exp(-j\pi k) \exp\left(-\frac{j2\pi kn}{N}\right). \end{aligned} \tag{2.47}$$

For k odd, $\exp(-j\pi k) = -1$, and the value of the clipping noise is equal to:

$$\begin{aligned} X_c^n(k) &= \sum_{\substack{n=0 \\ x[n+\frac{N}{2}]\geq 0}}^{\frac{N}{2}-1} x[n+\frac{N}{2}]\ \exp\left(-\frac{j2\pi kn}{N}\right) \\ &+ \sum_{\substack{n=0 \\ x[n+\frac{N}{2}]<0}}^{\frac{N}{2}-1} x[n+\frac{N}{2}]\ \exp\left(-\frac{j2\pi kn}{N}\right)\ ;\ k: odd. \end{aligned} \tag{2.48}$$

Now, changing the variable in the first term and replacing $x[n+\frac{N}{2}] = -x[n]$ in the second term of (2.48) gives:

$$\begin{aligned} X_c^n(k) &= \sum_{\substack{n=\frac{N}{2} \\ x[n]\geq 0}}^{N-1} x[n]\ \exp\left(-\frac{j2\pi k(n-\frac{N}{2})}{N}\right) \\ &- \sum_{\substack{n=0 \\ x[n]\geq 0}}^{\frac{N}{2}-1} x[n]\ \exp\left(-\frac{j2\pi kn}{N}\right) \\ &= -\sum_{\substack{n=\frac{N}{2} \\ x[n]\geq 0}}^{N-1} x[n]\ \exp\left(-\frac{j2\pi kn}{N}\right) \\ &- \sum_{\substack{n=0 \\ x[n]\geq 0}}^{\frac{N}{2}-1} x[n]\ \exp\left(-\frac{j2\pi kn}{N}\right) = -X_c(k)\ ;\ k: odd. \end{aligned} \tag{2.49}$$

Therefore from (2.45), it can be concluded that,

$$X(k) = 2X_c(k)\ ;\ k: odd, \tag{2.50}$$

or:

$$X_c(k) = \frac{X(k)}{2} \ ; \ k : odd. \tag{2.51}$$

For k even, from (2.45) and considering (2.37):

$$X_c(k) = X_c^n(k) \ ; \ k : even, \tag{2.52}$$

Therefore, from (2.51) and (2.52):

$$X_c(k) = \begin{cases} \frac{X(k)}{2} & \text{if } k \text{ odd} \\ X_c^n(k) & \text{if } k \text{ even} \end{cases} . \tag{2.53}$$

The final result in (2.53) shows that the amplitudes of odd subcarriers that carry data in the clipped signal are equal to half of their original amplitudes before clipping and all the clipping noise falls on even subcarriers.

Figure 2.19 displays the time anti-symmetry and orthogonal clipping noise for an example of ACO-OFDM symbol, where odd subcarriers take their values from 16 QAM constellation points. It can also be seen in Fig. 2.19 (b) that for ACO-OFDM, when only odd subcarriers are modulated, the time samples have anti-symmetry property as (2.41). Furthermore, as also proved in (2.53), the anti-symmetry leads to the clipping noise which is orthogonal to the data. A comparison between the corresponding amplitudes of the original data in Fig. 2.19 (a) and twice the values of clipped signal in Fig. 2.19 (d), also verifies the results in (2.53).

Notice that clipping the non-negative amplitudes in ACO-OFDM only guarantees non-negativity of the samples not the interpolated continuous signal.

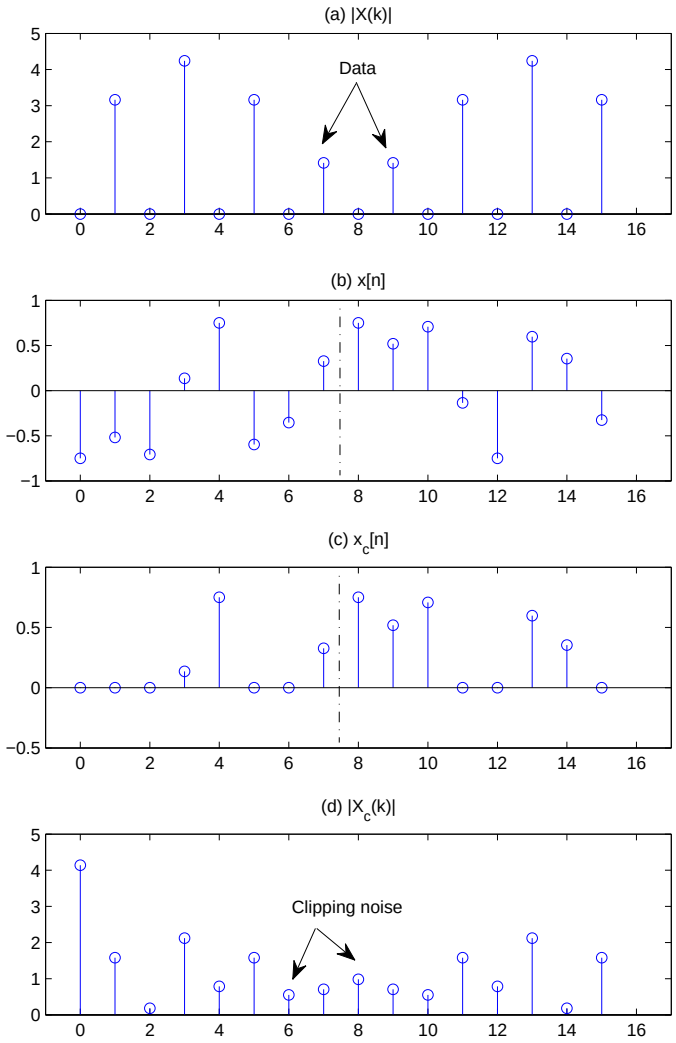

Figure 2.19: Example of signals in ACO-OFDM: (a) ACO-OFDM data loaded in frequency domain, (b) anti-symmetrical ACO-OFDM time samples, (c) clipped ACO-OFDM time samples, and (d) frequency components of the clipped ACO-OFDM.

2.6.3 Pulse Amplitude Modulated Discrete Multi-tone (PAM-DMT)

In PAM-DMT, similar to ACO-OFDM, a constraint is imposed on the subcarriers [49]. But unlike ACO-OFDM, only the imaginary parts of all subcarriers are modulated and the real components are set to zero. Thus:

$$X(k) = jC_k; \quad k = 0, 1, \cdots, N-1, \tag{2.54}$$

where C_k are chosen from PAM symbols assigned with Hermitian symmetry. The nth time sample can be found from IFFT on the subcarrier values,

$$x[n] \;=\; \frac{1}{N}\sum_{k=0}^{N-1} X(k)\exp\left(\frac{j2\pi kn}{N}\right); \quad n = 0, 1, \cdots, N-1. \tag{2.55}$$

By taking the Hermitian symmetry into account, $X(k) = X^*(N-k)$, $X(0) = X(\frac{N}{2}) = 0$, and changing the indices, (2.55) can be written as:

$$\begin{aligned}
x[n] &= \frac{1}{N}\left(\sum_{k=0}^{\frac{N}{2}-1} jC_k\ \exp\left(\frac{j2\pi kn}{N}\right) + \sum_{k=\frac{N}{2}}^{N-1}(-j)C_{N-k}\ \exp\left(\frac{j2\pi kn}{N}\right)\right) \\
&= \frac{1}{N}\left(\sum_{k=0}^{\frac{N}{2}-1} jC_k\ \exp\left(\frac{j2\pi kn}{N}\right) + \sum_{k=1}^{\frac{N}{2}}(-j)C_k\ \exp\left(\frac{j2\pi(N-k)n}{N}\right)\right) \\
&= \frac{1}{N}\sum_{k=1}^{\frac{N}{2}-1} C_k\ \left(j\ \exp\left(\frac{j2\pi kn}{N}\right) - j\ \exp\left(-\frac{j2\pi kn}{N}\right)\right) \\
&= \frac{-2}{N}\sum_{k=1}^{\frac{N}{2}-1} C_k\ \sin\left(\frac{2\pi kn}{N}\right).
\end{aligned} \tag{2.56}$$

Forming $x\left[\frac{N}{2}+n\right]$ and $x\left[\frac{N}{2}-n\right]$,

$$\begin{aligned} x\left[\frac{N}{2}+n\right] &= \frac{-2}{N}\sum_{k=1}^{\frac{N}{2}-1} C_k \ \sin\left(\frac{2\pi k(\frac{N}{2}+n)}{N}\right) \\ &= \frac{-2}{N}\sum_{k=1}^{\frac{N}{2}-1} C_k \ \sin\left(k\pi+\frac{2k\pi n}{N}\right), \\ x\left[\frac{N}{2}-n\right] &= \frac{-2}{N}\sum_{k=1}^{\frac{N}{2}-1} C_k \ \sin\left(\frac{2\pi k(\frac{N}{2}-n)}{N}\right) \\ &= \frac{-2}{N}\sum_{k=1}^{\frac{N}{2}-1} C_k \ \sin\left(k\pi-\frac{2k\pi n}{N}\right). \end{aligned} \tag{2.57}$$

From (2.57), and since for any k, $\sin\left(k\pi+\frac{2k\pi n}{N}\right) = -\sin\left(k\pi-\frac{2k\pi n}{N}\right)$, it can be concluded that the bipolar time samples in PAM-DMT also have anti-symmetry as,

$$x\left[\frac{N}{2}+n\right] = -x\left[\frac{N}{2}-n\right] \ ; \quad n=0,1,\cdots,\frac{N}{2}-1, \tag{2.58}$$

which can also be expressed as:

$$x\left[N-n\right] = -x[n] \ ; \quad n=0,1,\cdots,N. \tag{2.59}$$

Similar to ACO-OFDM, it is concluded that clipping the negative amplitudes does not lead to loss of information since the data can be extracted from the corresponding positive values. As a result, assume the clipped signal $x_c[n]$, and the value of the kth subcarrier of the clipped signal $X_c(k)$, to be defined as in (2.42) and (2.43). Also similar to ACO-OFDM, from (2.45),

$$X_c(k) = X(k) + X_c^n(k), \tag{2.60}$$

where:

$$X_c^n(k) = \sum_{\substack{n=0 \\ x[n]<0}}^{N-1} -x[n] \exp\left(-\frac{j2\pi kn}{N}\right). \tag{2.61}$$

Substituting (2.59) in (2.61), and changing the indices yields,

$$\begin{aligned} X_c^n(k) &= \sum_{\substack{n=0 \\ x[N-n]\geq 0}}^{N-1} -x[n] \exp\left(-\frac{j2\pi kn}{N}\right) \\ &= \sum_{\substack{n=0 \\ x[N-n]\geq 0}}^{N-1} x[N-n] \exp\left(-\frac{j2\pi kn}{N}\right) \\ &= \sum_{\substack{n=0 \\ x[n]\geq 0}}^{N-1} x[n] \exp\left(-\frac{j2\pi k(N-n)}{N}\right) \\ &= \sum_{\substack{n=0 \\ x[n]\geq 0}}^{N-1} x[n] \exp\left(\frac{j2\pi kn}{N}\right). \end{aligned} \tag{2.62}$$

Therefore, $X_c^n(k)$ can be separated to its real and imaginary part as,

$$\begin{aligned} Re\{X_c^n(k)\} &= \sum_{\substack{n=0 \\ x[n]\geq 0}}^{N-1} x[n] \cos\left(\frac{2\pi kn}{N}\right), \\ Im\{X_c^n(k)\} &= \sum_{\substack{n=0 \\ x[n]\geq 0}}^{N-1} x[n] \sin\left(\frac{2\pi kn}{N}\right). \end{aligned} \tag{2.63}$$

Notice also that from (2.43), $X_c(k)$ can be separated to real and imaginary parts as,

$$\begin{aligned} Re\{X_c(k)\} &= \sum_{\substack{n=0 \\ x[n]\geq 0}}^{N-1} x[n]\ \cos\left(\frac{2\pi kn}{N}\right), \\ Im\{X_c(k)\} &= -\sum_{\substack{n=0 \\ x[n]\geq 0}}^{N-1} x[n]\ \sin\left(\frac{2\pi kn}{N}\right). \end{aligned} \tag{2.64}$$

Comparing (2.63) and (2.64) gives:

$$\begin{aligned} Re\{X_c^n(k)\} &= Re\{X_c(k)\}, \\ Im\{X_c^n(k)\} &= -Im\{X_c(k)\}. \end{aligned} \tag{2.65}$$

Replacing (2.54) and (2.66) in (2.60) yields:

$$\begin{aligned} Im\{X_c(k)\} &= \frac{C_k}{2}, \\ Re\{X_c(k)\} &= Re\{X_c^n(k)\}. \end{aligned} \tag{2.66}$$

Therefore, it is concluded that the imaginary part of the clipped signal in frequency is exactly equal to half of the imaginary part of the original signal before clipping hence clipping noise only falls on real parts of the subcarriers.

The corresponding subcarrier components for the original signal and clipped signal are displayed in Fig. 2.20. The time anti-symmetry in PAM-DMT is also shown in Fig. 2.21. It can be seen in Fig. 2.20 (d) that the imaginary components of the clipped signal are correspondent to the imaginary part of the original signal in Fig. 2.20 (b). Therefore, the clipping noise must fall on real part of the subcarriers as shown in Fig. 2.20 (c).

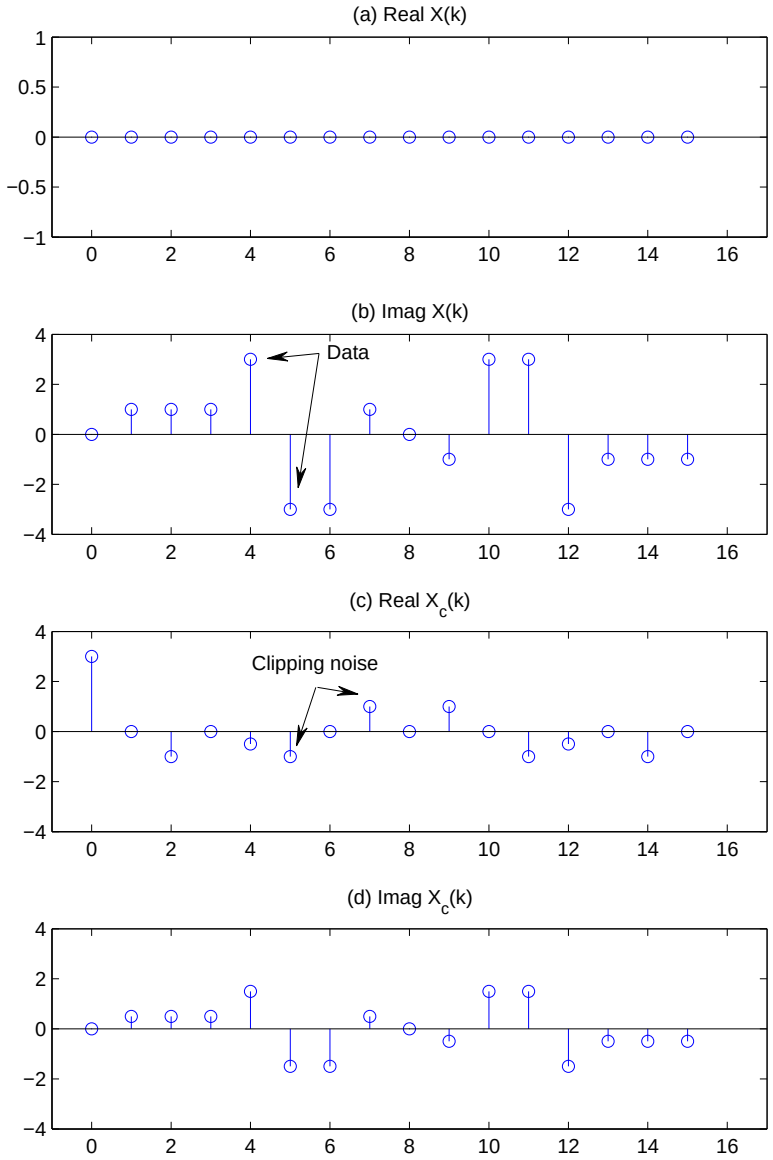

Figure 2.20: Example of PAM-DMT signals in frequency: (a) PAM-DMT loaded in real part of the frequency domain, (b) PAM-DMT loaded in imaginary part of the frequency domain, (c) real part of the frequency components of the clipped PAM-DMT, and (d) imaginary part of the frequency components of the clipped PAM-DMT.

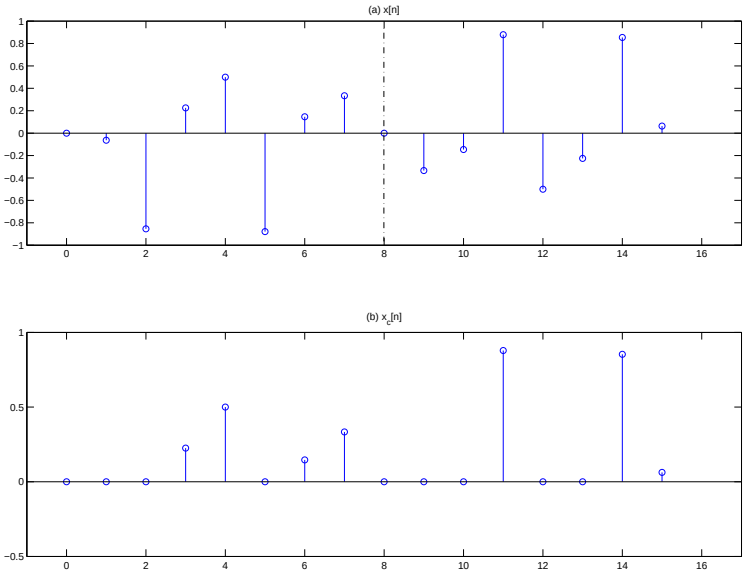

Figure 2.21: Example of PAM-DMT signals in time: (a) anti-symmetrical PAM-DMT time samples, and (b) clipped PAM-DMT time samples.

Similar to ACO-OFDM, clipping the non-negative amplitudes in PAM-DMT only guarantees non-negativity of the samples not the continuous signal.

2.7 Conclusion

In this chapter, orthogonal frequency division multiplexing is suggested as a method of choice for implementation on low bandwidth VLC channels with adequate SNRs. The proposed OFDM methods for applying on IM/DD channels are then presented. It is shown that ACO-OFDM and PAM-DMT achieve the same error performance in flat channels [49]. Also, they provide better optical power efficiency compared to DC-biased OFDM since they do not require a DC bias to guarantee non-negativity of the transmitted signal [44, 45, 46, 49]. However, only half the degrees of freedom

are available for data modulation in both techniques. Notice that ACO-OFDM does not modulate even subcarriers and PAM-DMT does not have data on real parts of the subcarriers. This is inefficient as all the subcarriers can take complex values for data transmission. Furthermore, ACO-OFDM and PAM-DMT only guarantee non-negativity of the samples not the continuous OFDM time signal that is transmitted through the channel. As it will also be discussed in Chapter 3, ACO-OFDM and PAM-DMT suffer from their large peak-to-average-power ratio.

In the next chapter, a novel framework for OFDM signaling on IM/DD channels is established. The proposed system uses complex values for all subcarriers. The peak-to-average-power ratio is reduced accordingly. Furthermore, the non-negativity of the continuous OFDM signal is guaranteed by applying such technique.

Chapter 3

Spectrally Factorized Optical OFDM

In the previous chapter, the proposed OFDM designs for IM/DD channels are presented. It is pointed out that ACO-OFDM and PAM-DMT offer better error performance compared to DC-biased OFDM but lose half the carriers to satisfy non-negativity. In this chapter, spectrally factorized optical OFDM (SFO-OFDM) is introduced as the framework to implement OFDM on IM/DD optical channels.

In Sec. 3.1, the framework of SFO-OFDM is established by proving two theorems. The results are then used in Sec. 3.2 for designing signal sets. Finally, the performance of SFO-OFDM in IM/DD channels is presented and compared with other techniques in Sec. 3.3.

3.1 System Model

3.1.1 Channel Model

Although the practical channels are frequency selective and have limited bandwidth, in this work for simplicity, it is assumed that the channel is approximately flat with unlimited bandwidth. The noise $z(t)$ in the channel model (2.9) can then be modeled as zero mean additive white Gaussian distributed.

The optical signal-to-noise ratio, SNR_o, peak-to-average power ratio, $PAPR$, and peak-signal-to noise ratio, $PSNR$, are defined as in (2.22), (2.13), and (2.25) respectively.

3.1.2 Spectral Factorization

The concept of spectral factorization is well studied in FIR filter design [85]. Here, this concept will be considered from another point of view, namely to construct positive amplitude OFDM signals appropriate for transmission on IM/DD channels.

Theorem 1. *Any periodic, band-limited, real and positive time signal has Fourier series coefficients which form an autocorrelation sequence.*

Proof. Let $x(t)$ be a periodic, band-limited, real and positive time signal with Fourier series coefficients a_l. Thus,

$$x(t) = \sum_{l=-K}^{K} a_l \; e^{jl\omega_0 t} > 0, \tag{3.1}$$

where $\omega_0 = \frac{2\pi}{T}$, T is the period of the signal and $N = 2K + 1$ is the number of the

coefficients. Since $x(t)$ is real, the coefficients a_l have Hermitian symmetry, i.e.,

$$\forall l : a_{-l}^{*} = a_l. \tag{3.2}$$

As suggested in [85], define

$$T(z) = \sum_{l=-K}^{K} a_l \; z^l, \tag{3.3}$$

as the general z-domain characteristic function. Notice that $x(t)$ is the special case of $T(z)$ when $z = e^{j\omega_0 t}$, i.e. z is located on the unit circle:

$$x(t) = T\left(e^{j\omega_0 t}\right). \tag{3.4}$$

Replacing z with $1/z^*$ in (4.11) yields:

$$T\left(\frac{1}{z^*}\right) = \sum_{l=-K}^{K} a_l \; (z^*)^{-l} = \left(\sum_{l=-K}^{K} a_l^* \; z^{-l}\right)^* . \tag{3.5}$$

Changing the indices in (3.5) and using (3.2) gives,

$$T\left(\frac{1}{z^*}\right) = \left(\sum_{l=-K}^{K} a_{-l}^* \; z^l\right)^* = \left(\sum_{l=-K}^{K} a_l \; z^l\right)^* = T^*(z). \tag{3.6}$$

Therefore,

$$T^*\left(\frac{1}{z^*}\right) = T(z). \tag{3.7}$$

Notice from (3.7) that the roots of $T(z)$ appear conjugate reciprocally, i.e. if λ_i is a root of $T(z)$ outside the unit circle, $1/\lambda_i^*$ is also a root of $T(z)$ inside the unit circle.

Moreover, since the conjugate reciprocal of a point on the unit circle is itself, and the total number of zeros is $2K$ which is even, $T(z)$ can also have even number of zeros on the unit circle. As a result, $T(z)$ can be written in terms of its zeros as

$$T(z) = c\ z^{-K} \prod_{l=1}^{J} (z - e^{j\phi_l}) \prod_{i=1}^{K-J/2} (z - \lambda_i) \left(z - \frac{1}{\lambda_i^*} \right), \tag{3.8}$$

in which c is a scaling factor and ϕ_l are the phase of zeros on the unit circle. Without loss of generality, assume that the λ_i are the zeros outside the unit circle.

Consider the case of zeros on the unit circle ($J > 0$). Since $x(t) = T(e^{j\omega_0 t})$ implies that $x(t) = 0$ for $t = \phi_l/\omega_0$, which is a contradiction. Consequently, the positivity of $x(t)$ implies that $T(z)$ has no zeros on the unit circle, i.e.,

$$T(z) = c\ z^{-K} \prod_{i=1}^{K} (z - \lambda_i) \left(z - \frac{1}{\lambda_i^*} \right). \tag{3.9}$$

Rearranging,

$$\begin{aligned} T(z) &= \underbrace{\left(\frac{c\ (-1)^K}{\prod_{i=1}^{K} (\lambda_i^*)} \right)}_{c'} \underbrace{\prod_{i=1}^{K} (1 - \lambda_i z^{-1})}_{H(z)} \underbrace{\prod_{i=1}^{K} (1 - \lambda_i^* z)}_{H^*\left(\frac{1}{z^*}\right)} \\ &= c' H(z)\ H^* \left(\frac{1}{z^*} \right). \end{aligned} \tag{3.10}$$

From (3.7), $c' = (c')^*$, i.e. c' is real. Moreover, $\forall t$, $x(t) = T(e^{j\omega_0 t}) > 0$. Thus from

(3.10),

$$\forall t : x(t) = T(e^{j\omega_0 t}) = c' \underbrace{\prod_{i=1}^{K} \mid 1 - \lambda_i e^{-j\omega_0 t} \mid^2}_{x'(t)} > 0. \tag{3.11}$$

Since $T(z)$ has no zeros on the unit circle, $x'(t) > 0$ therefore, $c' > 0$ and has a square root. Simplifying (3.10),

$$T(z) = \underbrace{\left(\sqrt{c'} H(z)\right)}_{S(z)} \underbrace{\left(\sqrt{c'} H^*\left(\frac{1}{z^*}\right)\right)}_{S^*\left(\frac{1}{z^*}\right)} = S(z)\ S^*\left(\frac{1}{z^*}\right). \tag{3.12}$$

Let

$$S(z) = \sum_{l=0}^{K} s_l\ z^{-l}. \tag{3.13}$$

Substituting (3.13) into (3.12) and comparing with (4.11) gives,

$$\begin{aligned} \sum_{l=-K}^{K} a_l\ z^l &= \left(\sum_{l=0}^{K} s_l\ z^{-l}\right)\left(\sum_{l=0}^{K} s_l^*\ z^l\right) \\ &= \sum_{l=-K}^{K}\left(\sum_{m=0}^{K} s_m s_{m-l}^*\right) z^l, \end{aligned} \tag{3.14}$$

which results in:

$$a_l = \sum_{m=0}^{K} s_m s_{m-l}^*. \tag{3.15}$$

Thus, a_l is the autocorrelation of s_l.

□

Theorem 2. *If the Fourier series coefficients of a periodic band-limited signal $f(t)$ form an autocorrelation sequence, then $\forall t\ f(t) \geq 0$.*

Proof. Let b_l be the Fourier series coefficients of the periodic, band-limited signal $f(t)$. Assume that the sequence b_l is an autocorrelation of some sequence g_l, $l \in [-K, K]$ as,

$$b_l = \sum_{m=0}^{K} g_m g_{m-l}^* = g_l \star g_{-l}^*, \tag{3.16}$$

where $\star$ denotes convolution. From the Fourier series properties, $g_l \star g_{-l}^*$ are the Fourier series coefficients of the signal

$$f(t) = g(t)g^*(t) = \|g(t)\|^2. \tag{3.17}$$

Thus, $f(t) = \|g(t)\|^2$ is real and non-negative for all time. □

3.2 System Design

3.2.1 Design Scheme

In SFO-OFDM, the autocorrelation of frequency coefficients in (3.12) is used to produce unipolar signals directly without constraining the modulation bandwidth. In particular, the subcarrier amplitudes are chosen such that they form an autocorrelation sequence, which was shown in Sec. 3.1.2 to be necessary and sufficient to guarantee amplitude positivity. The autocorrelation sequences are generated by sub-optimally designing their z-plane zeros.

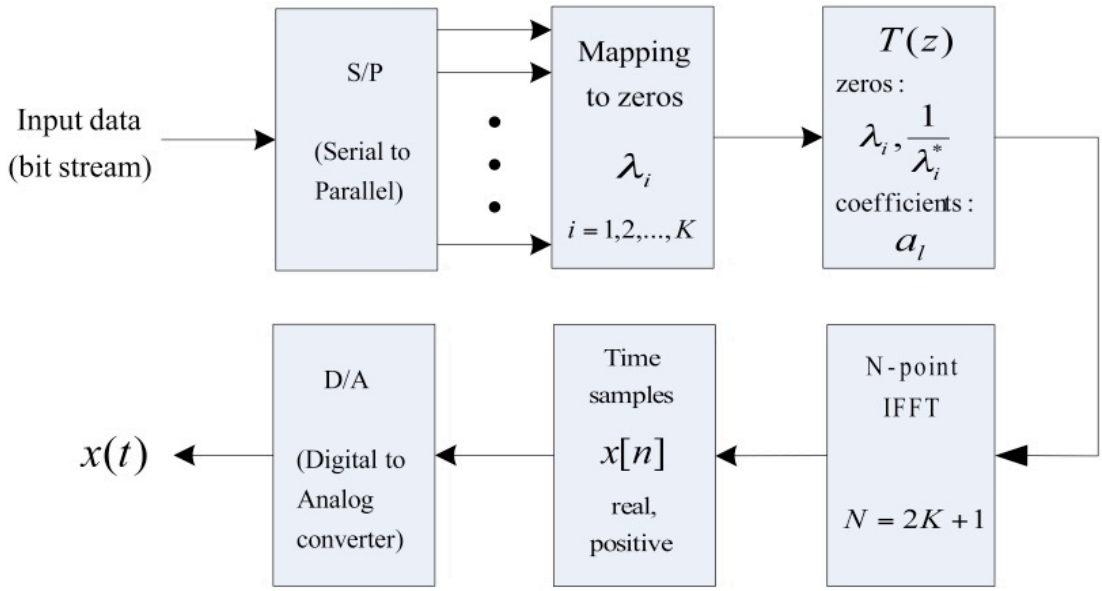

Figure 3.1: Block diagram of the SFO-OFDM transmitter.

Figure 3.1 shows a simple block diagram of the SFO-OFDM transmitter. The input serial data is partitioned into parallel blocks which are mapped to the zeros of $S(z)$ which lie outside the unit circle, i.e., λ_i. The characteristic z-domain function $T(z) = S(z)\ S^*\left(\frac{1}{z^*}\right)$ is then formed with conjugate reciprocal pair zeros λ_i and $1/\lambda_i^*$ to generate the autocorrelation coefficients a_l. Performing an $N = 2K+1$ point IDFT on the coefficients of $T(z)$ produces a positive time sequence $x[n]$. Finally, a positive OFDM signal $x(t)$ which contains one period of the periodic signal in time is generated using the time samples $x[n]$.

The only question left to be answered is which zero sets to choose for data modulation. The answer to this question will be followed in Sec. 3.2.2 and Sec. 3.2.3.

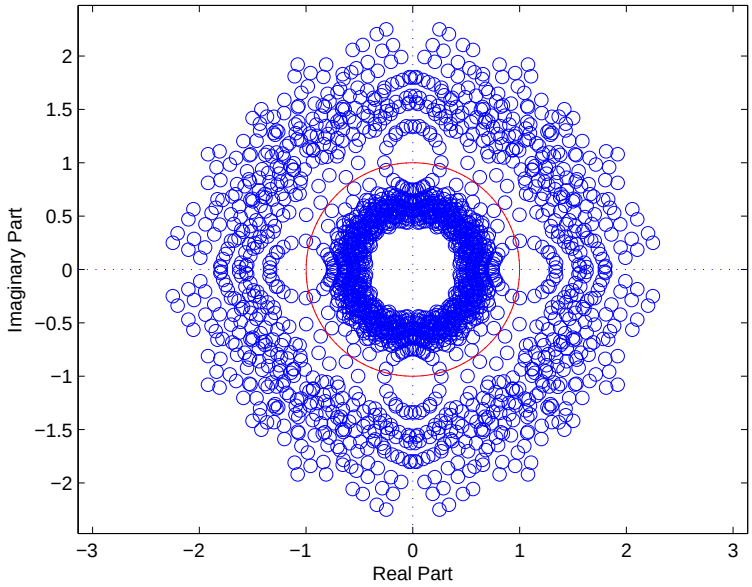

Figure 3.2: Distribution of the possible zeros of DC Biased OFDM with 9 subcarriers and 8 bits per symbol. Unit circle shown in red.

3.2.2 DC-biased OFDM in SFO-OFDM framework

Since DC-biased OFDM signals are band-limited positive signals, they can be represented by the zeros of the characteristic function $T_{DC}(z)$. From Theorem 1, the Fourier series coefficients of DC-biased time signals must form an autocorrelation sequence. Figure 3.2 shows the z-plane distribution of the possible zeros for $T_{DC}(z)$ when 9 subcarriers are used with the DC subcarrier adjusted to ensure positivity and 4-QAM all other subcarriers assigned with Hermitian symmetry.

Notice that all zeros outside the unit circle have magnitude $r_1 = 1 < r < r_2 = 2.5$. As zeros appear in conjugate reciprocal pairs, there are two zero-empty regions $r > 2.5$ and $r < 0.4$. Moreover, simulation results show that by increasing the bias added to the DC subcarrier, the outside unit circle zeros move away from the unit circle, i.e. r_1, r_2 increase. Qualitatively, to have better optical efficiency the λ_i should be chosen

close to the unit circle, which will be formalized in the next section.

3.2.3 Relating λ_i to average optical power

Notice that the average optical power of the transmitted signal $x(t)$ is the DC term a_0. Using (3.15) yields,

$$P_{ave} = a_0 = \|s_0\|^2 + \|s_1\|^2 + \cdots + \|s_K\|^2. \tag{3.18}$$

Assume $S(z)$ has K zeros, denoted $\lambda_i = r_i\ e^{j\theta_i}$. For simplicity assume K is even, however, all the conclusions are trivially extended in the case of K odd. Using (3.10), P_{ave} can be written as,

$$P_{ave} = \frac{c(-1)^K}{\prod_{i=1}^{K}\lambda_i^*}\left\{1 + \left\|\sum_{i=1}^{K}\lambda_i\right\|^2 + \left\|\sum_{i=1,k>i}^{K}\lambda_i\lambda_k\right\|^2 + \cdots + \left\|\prod_{i=1}^{K}\lambda_i\right\|^2\right\}. \tag{3.19}$$

From Thm. 1, $c' > 0$ and hence $P_{ave} > 0$. Notice that for any set of λ_i, c can be chosen such that P_{ave} takes any positive value. Therefore, define $P_{norm} = |P_{ave}/c|$, i.e.,

$$P_{norm} = \underbrace{\frac{1}{\left\|\prod_{i=1}^{K}\lambda_i^*\right\|}}_{f_0(\lambda_1,\lambda_2,\ldots,\lambda_K)} + \underbrace{\frac{\left\|\sum_{i=1}^{K}\lambda_i\right\|^2}{\left\|\prod_{i=1}^{K}\lambda_i^*\right\|}}_{f_1(\lambda_1,\lambda_2,\ldots,\lambda_K)} + \underbrace{\frac{\left\|\sum_{i=1,k>i}^{K}\lambda_i\lambda_k\right\|^2}{\left\|\prod_{i=1}^{K}\lambda_i^*\right\|}}_{f_2(\lambda_1,\lambda_2,\ldots,\lambda_K)} + \cdots + \underbrace{\frac{\left\|\prod_{i=1}^{K}\lambda_i\right\|^2}{\left\|\prod_{i=1}^{K}\lambda_i^*\right\|}}_{f_K(\lambda_1,\lambda_2,\ldots,\lambda_K)} \tag{3.20}$$

In order to increase the power efficiency, the λ_i are selected to minimize P_{norm}.

Notice that a rotation of the λ_i does not change P_{norm}. That is, if the set of zeros $\lambda_i = r_i\ e^{j\theta_i}$ have $P_{norm} = P_0$, the set of zeros $\lambda_i' = r_i\ e^{j(\theta_i+\phi)}$ leads to the the same $P_{norm} = P_0$. Moreover, for any $m = 0, 1, ..., \frac{K}{2}$

$$f_m\left(\frac{1}{\lambda_1^*}, \frac{1}{\lambda_2^*}, ..., \frac{1}{\lambda_K^*}\right) = f_{K-m}(\lambda_1, \lambda_2, ..., \lambda_K). \tag{3.21}$$

Define $\vec{r}$ and $\vec{\theta}$ as vectors of the magnitude and phase of each λ_i, $i = 1, \ldots, K$. Then the property (3.21) can be denoted,

$$f_m(\vec{r}^{-1}, \vec{\theta}) = f_{K-m}(\vec{r}, \vec{\theta}) \tag{3.22}$$

where $\vec{r}^{-1}$ is the element-wise reciprocal of $\vec{r}$. Rewriting (3.20) using the notation of (3.22) gives,

$$P_{norm} = \sum_{m=0}^{\frac{K}{2}-1} \left(f_m(\vec{r}, \vec{\theta}) + f_m(\vec{r}^{-1}, \vec{\theta})\right) + \frac{1}{2}\left(f_{\frac{K}{2}}(\vec{r}, \vec{\theta}) + f_{\frac{K}{2}}(\vec{r}^{-1}, \vec{\theta})\right). \tag{3.23}$$

The critical points of the smooth function P_{norm} are located where the gradient with respect to each r_i and θ_i is zero. Thus for the r_i,

$$\begin{aligned} \frac{\partial P_{norm}}{\partial r_i} &= \sum_{m=0}^{\frac{K}{2}-1} \left(\frac{\partial f_m(\vec{r}, \vec{\theta})}{\partial r_i} - \frac{\partial f_m(\vec{r}^{-1}, \vec{\theta})}{\partial r_i} \cdot \frac{1}{r_i^2}\right) \\ &+ \frac{1}{2}\left(\frac{\partial f_{\frac{K}{2}}(\vec{r}, \vec{\theta})}{\partial r_i} - \frac{\partial f_{\frac{K}{2}}(\vec{r}^{-1}, \vec{\theta})}{\partial r_i} \cdot \frac{1}{r_i^2}\right) = 0. \end{aligned} \tag{3.24}$$

Since (3.24) has the same form for every r_i, if a zero exists for some $r_i = r$, it must also be a critical point for all r_i, $i = 1, \ldots, K$. That is, placing the λ_i lie on a ring of

radius $r > 1$ is a critical point of P_{norm} which is termed $P_{\text{norm}}^{\text{ring}}$. In this case, P_{norm} in (3.20) can be simplified to

$$P_{\text{norm}}^{\text{ring}} = \frac{\overbrace{1}^{b_0}}{r^K} + \frac{\overbrace{\left\|\sum_{i=1}^{K} e^{j\theta_i}\right\|^2}^{b_1} r^2}{r^K} + \cdots + \frac{\overbrace{\left\|e^{j\left(\sum_{i=1}^{K}\theta_i\right)}\right\|^2}^{b_K} r^{2K}}{r^K}. \tag{3.25}$$

Using Cauchy-Schwarz inequality,

$$P_{\text{norm}}^{\text{ring}} = b_{K/2} + \sum_{m=0}^{\frac{K}{2}-1} b_m \left(r^{2m-K} + \frac{1}{r^{2m-K}}\right) \geq b_{K/2} + 2\sum_{m=0}^{\frac{K}{2}-1} b_m, \tag{3.26}$$

and the equality occurs when $r = 1$. In other words, the unit circle is the global minimum of $P_{\text{norm}}^{\text{ring}}$ in (3.26).

3.2.4 Design Characterization

Since P_{norm} has a minimum when the λ_i are chosen on the unit circle, the K zeros of the proposed SFO-OFDM system are chosen on a ring $r = 1 + \epsilon$ for some small $\epsilon > 0$. Notice that in DC-biased OFDM, placing λ_i near the unit circle also improves optical power efficiency.

The λ_i are chosen according to the criterion of maximizing the minimum euclidean distance between the corresponding time sequences. The ring $r = 1 + \epsilon$ is partitioned into C equally spaced points. Define $\mathcal{C}$ as the set of all $\binom{C}{K}$ possible zero configurations in which C is chosen such that $\binom{C}{K} \geq 2^M$. To send M bits, an initial random set, $\mathcal{B}$, of 2^M possible polynomials are selected from $\mathcal{C}$ and the minimum distance, d_{min}, between any pair of time sequences is computed. Then, another configuration from

$\alpha \in \mathcal{C}$ is selected and if the minimum distance to all configurations in $\mathcal{B}$ is larger than d_{min}, it replaces an element in $\mathcal{B}$. This process is repeated with all other possible configurations in $\mathcal{C}$.

The value for C is determined by the desired error performance of the system. Clearly, increasing C leads to an improvement in the performance, however, determining the optimal 2^M polynomials form $\binom{C}{K}$ possible cases is extremely time consuming. It should be noted that the process of finding the optimal zero sets for $\mathcal{C}$ can be done offline. Once $\mathcal{C}$ is found, the time samples can be stored and used for transmission through the channel.

3.3 Performance of SFO-OFDM

Assume that $M = 8$ bits are transmitted with $N = 9$ subcarriers. In DC-biased OFDM, 4 subcarriers carry 4-QAM, whereas in ACO-OFDM, 2 odd subcarriers carry 16-QAM. For the SFO-OFDM, $C = 48$, $r = 1.0001$. At the receiver, a maximum likelihood detector is used. The Euclidean distance between the received time sequence and all possible time sequences is exhaustively compared and the sequence which minimizes the distance is selected. This is a complex operation which is only suitable for small to moderate numbers of subcarriers.

Figure 3.3 shows the BER of SFO-OFDM, DC-biased OFDM and ACO OFDM versus SNR_o. It can be seen that SFO-OFDM outperforms DC-biased OFDM and has approximately 0.5 dB better performance than ACO-OFDM at $BER = 10^{-5}$. Simulation results verify that performance improves as r approaches the unit circle.

In addition, for this example the PAPR, $\text{PAPR}_{ACO}/\text{PAPR}_{SFO} = 1.3023$. Therefore, SFO-OFDM signals have 30% less PAPR than ACO-OFDM for $M = 8$ and

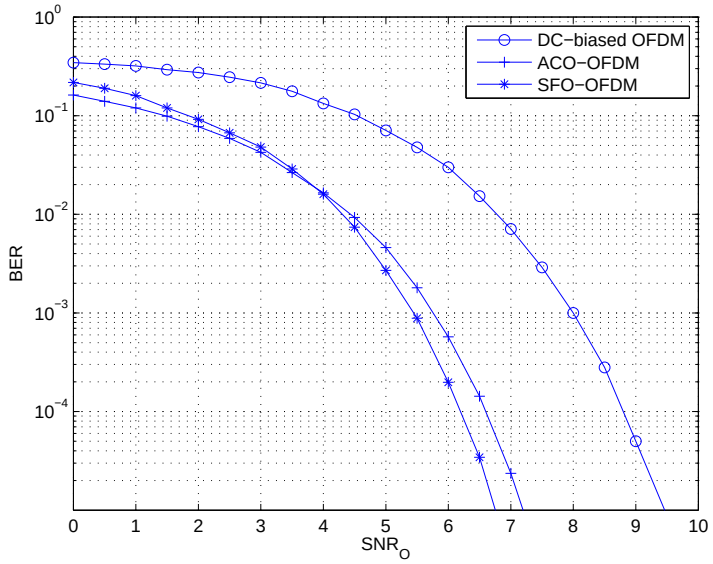

Figure 3.3: BER versus optical SNR for DC-biased OFDM, ACO-OFDM and SFO-OFDM ; $M = 8$, $N = 9$, $C = 48$, $r = 1.0001$

$N = 9$ and may result in simpler transmitter design.

Figure 3.4 shows the BER of SFO-OFDM, DC-biased OFDM and ACO-OFDM where the constraint is imposed on the peak of the transmitted signal. It can be seen in Fig. 3.4 that ACO-OFDM has the worst performance in terms of PSNR compared to DC-biased OFDM and SFO-OFDM. Simulation results show that SFO-OFDM has approximately 0.75 dB better performance than DC-biased OFDM, and 1.7 dB better performance than ACO-OFDM at $BER = 10^{-5}$.

3.4 Conclusions

In this chapter, a novel bandwidth efficient method to implement OFDM on IM/DD channels is presented and termed *spectrally factorized optical* OFDM (SFO-OFDM).

Spectral factorization provides a formalism for non-negative multiple subcarrier

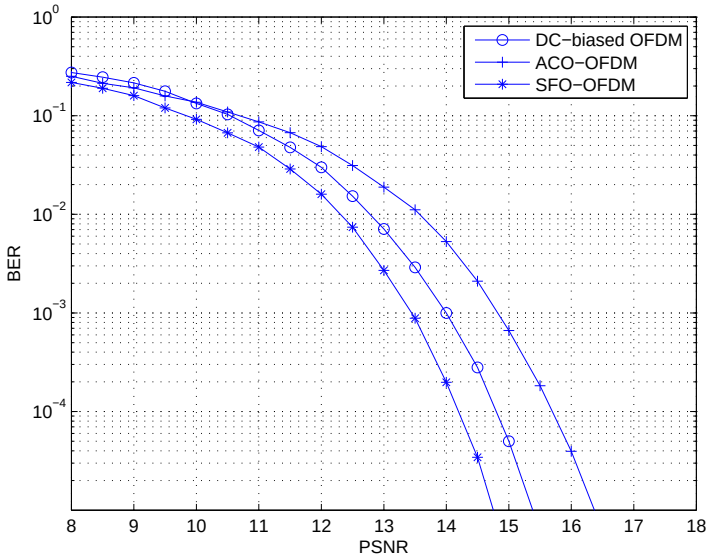

Figure 3.4: BER versus PSNR for DC-biased OFDM, ACO-OFDM and SFO-OFDM ; $M = 8$, $N = 9$, $C = 48$, $r = 1.0001$

modulation and can represent all band-limited OFDM signals for IM/DD channels. It is shown that a necessary and sufficient condition for a band-limited periodic signal to be positive for all time is that the frequency coefficients form an autocorrelation sequence. Therefore using spectral factorization, non-negative OFDM signals can be generated with no explicit bias. Instead of sending data directly on the subcarriers, the autocorrelation of the *complex* data sequence is performed before transmission to guarantee non-negativity. In z-domain, the average optical power is linked to the position of the zeros and used for the design of signal sets.

In contrast to previous approaches, SFO-OFDM is able to use the entire bandwidth for data transmission and does not require reserved subcarriers. Also, SFO-OFDM guarantees non-negativity of the continuous time signal whereas ACO-OFDM only guarantees non-negativity of the samples. Using a sub-optimal design technique

with 9 subcarriers and 8 bits per symbol, SFO-OFDM has a 0.5 dB gain over ACO-OFDM at a BER of 10^{-5} and a reduction in peak-to-average ratio of more than 30%. At the same BER, it is shown that SFO-OFDM has 0.75 dB and 1.7 dB peak gain over DC-biased OFDM and ACO-OFDM respectively.

However, the discussed advantages in SFO-OFDM are achieved at the expense of having a more complex receiver structure compared to ACO-OFDM and DC-biased OFDM systems. The fact that SFO-OFDM detects the time sequences jointly, makes the implementation of the SFO-OFDM receiver more complex than other proposed methods especially when the number of subcarriers is higher. There is room for improvement in the SFO-OFDM design presented in this chapter and this work serves as a first step to future designs.

Chapter 4

Receiver Design for Clipped Multi-Carrier Systems

In Chapter 3, a new OFDM modulation framework for IM/DD systems was proposed and shown to mitigate the drawbacks of ACO-OFDM and PAM-DMT while improving the optical power efficiency and peak-to-average power ratio.

In this chapter, a new receiver design for ACO-OFDM and PAM-DMT systems is devised. Previous receiver designs in [44, 48] ignore the clipping noise structure in detection and only rely on clipping the negative part of the received signal to improve the optical power efficiency. In this work, however, the structure of the clipping noise is used to implement a new detector. By observing the inherent time anti-symmetry of the signal, a pairwise maximum likelihood (ML) detector is developed and used to remove half of the noise power at the receiver. Simulation results verify that the proposed detection scheme improves the optical power efficiency of the system.

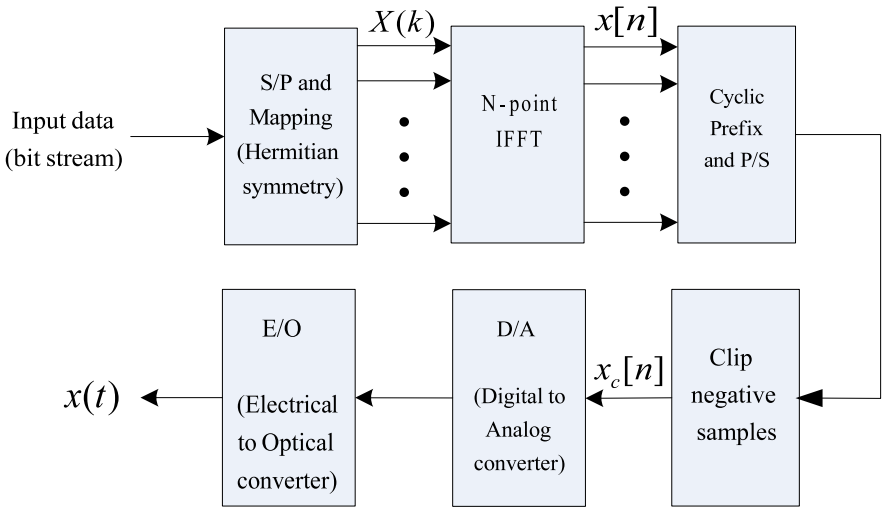

Figure 4.1: Block diagram of an ACO-OFDM or PAM-DMT transmitter.

4.1 System Model

Figure 4.1 displays the block diagram of an ACO-OFDM and PAM-DMT transmitter. The input serial data is first partitioned into parallel data streams in the S/P block. Each data stream is then mapped onto subcarrier values chosen from a certain constellation points assigned with Hermitian symmetry. As discussed in Chapter 2, in ACO-OFDM only odd subcarriers take values chosen from QAM constellation points, whereas in PAM-DMT, imaginary parts of the subcarriers are modulated from PAM constellation points. It was shown in (2.41) and (2.59) that the resulting time sequence, $x[n]$, after performing the IFFT is anti-symmetric satisfying

$$\begin{aligned} x_{ACO}\left[\frac{N}{2}+n\right] &= -x_{ACO}[n], \\ x_{PAM}\left[N-n\right] &= -x_{PAM}[n]. \end{aligned} \tag{4.1}$$

The negative amplitudes are then clipped to produce non-negative OFDM samples, $x_c[n]$, suitable for transmission through IM/DD channels. It was shown in both methods that clipping the negative part of the amplitudes does not lead to loss of information since the clipping noise is orthogonal to the data [44, 49]. After appending a cyclic extension, the clipped non-negative samples are passed through a digital to analog filter and converted to an optical signal, $x(t)$, using an LED.

4.1.1 Channel Model

To recover the transmitted data, it is assumed that the receiver knows the channel response and performs zero-forcing equalization (ZFE). The equalized received signal y in (2.9) can be written as,

$$y[n] = x_c[n] + z[n], \tag{4.2}$$

where $x_c[n]$ are the clipped non-negative transmitted samples. Notice that $z[n]$, the channel noise, is a zero mean colored noise with variance σ_z^2 and is equal to the convolution of the receiver front end filter $c[n]$, and additive white Gaussian noise $w[n]$. The receiver front end filter is chosen such that $c[n] * h[n] = \delta[n]$ where $h[n]$ is the channel impulse response. For the case of a flat channel, $c[n] = \delta[n]$ and $z[n]$ is white.

The optical signal to noise ratio, SNR_o, can then be defined as,

$$SNR_o = \frac{P_{ave}}{\sigma_z}, \tag{4.3}$$

where

$$P_{ave} = E\{x_c[n]\}, \tag{4.4}$$

is the average power of the transmitted signal.

4.1.2 Properties of ACO-OFDM and PAM-DMT

For a large number of subcarriers, the amplitude of the unclipped ACO-OFDM and PAM-DMT signal can be approximated by a Gaussian distribution [84]. Thus, the amplitude distribution of the clipped signal, $x_c[n]$, is the half-Gaussian

$$f_{x_c}(x) = 0.5\ \delta(x) + \frac{u(x)}{\sigma_x\sqrt{2\pi}}\ \exp\left(-\frac{x^2}{2\sigma_x^2}\right), \tag{4.5}$$

where σ_x is the standard deviation of the unclipped Gaussian distributed signal, $\delta(\cdot)$ is the Dirac delta function and $u(\cdot)$ is the Heaviside step function. The average transmitted power, P_{ave}, of the clipped signal in (4.4) is

$$P_{ave} \;=\; E\{x_c\} = \int_{-\infty}^{\infty} x f_{x_c}(x)\ dx = \frac{\sigma_x}{\sqrt{2\pi}}. \tag{4.6}$$

Figure 2.19 and 2.21 display the anti-symmetry structure of ACO-OFDM and PAM-DMT as in (4.1). Observe that the positive sample in both methods has a corresponding zero sample due to the clipping operation.

For compactness, define

$$\tilde{x}_c[n] = \begin{cases} x_c[n+N/2] & ; \quad \text{in ACO-OFDM} \\ x_c[N-n] & ; \quad \text{in PAM-DMT} \end{cases} . \tag{4.7}$$

Furthermore, define the pair $(x_c[n], \tilde{x}_c[n])$, $n \in 0, 1, 2, \ldots, N/2-1$. Consider the two possible scenarios (H_1 and H_2) that may arise for a given $x_c[n]$: (i) (H_1) $x_c[n] > 0$ and $\tilde{x}_c = 0$ or (ii) (H_2) $x_c[n] = 0$ and $\tilde{x}_c > 0$. The joint distribution of $x_c[n]$ and $\tilde{x}_c[n]$ is independent of n and can then be written as

$$f_{x_c,\tilde{x}_c}(x_1, x_2) \;=\; 0.5\; f_{x_c,\tilde{x}_c|H_1}(x_1, x_2) + 0.5\; f_{x_c,\tilde{x}_c|H_2}(x_1, x_2), \tag{4.8}$$

with the underlying assumption that $x[n]$ is Gaussian distributed. Furthermore, conditioned on H_1 or H_2 the distribution of $(x_c[n], \tilde{x}_c[n])$ is

$$\begin{aligned} f_{x_c,\tilde{x}_c|H_1}(x_1, x_2) &= \frac{2u(x_1)}{\sigma_x\sqrt{2\pi}} \exp\left(-\frac{x_1^2}{2\sigma_x^2}\right) \delta(x_2), \\ f_{x_c,\tilde{x}_c|H_2}(x_1, x_2) &= \frac{2u(x_2)}{\sigma_x\sqrt{2\pi}} \exp\left(-\frac{x_2^2}{2\sigma_x^2}\right) \delta(x_1). \end{aligned} \tag{4.9}$$

Replacing (4.9) in (4.8), leads to the joint distribution

$$\begin{aligned} f_{x_c,\tilde{x}_c}(x_1, x_2) &= \frac{u(x_1)}{\sigma_x\sqrt{2\pi}} \exp\left(-\frac{x_1^2}{2\sigma_x^2}\right) \delta(x_2) \\ &+ \frac{u(x_2)}{\sigma_x\sqrt{2\pi}} \exp\left(-\frac{x_2^2}{2\sigma_x^2}\right) \delta(x_1). \end{aligned} \tag{4.10}$$

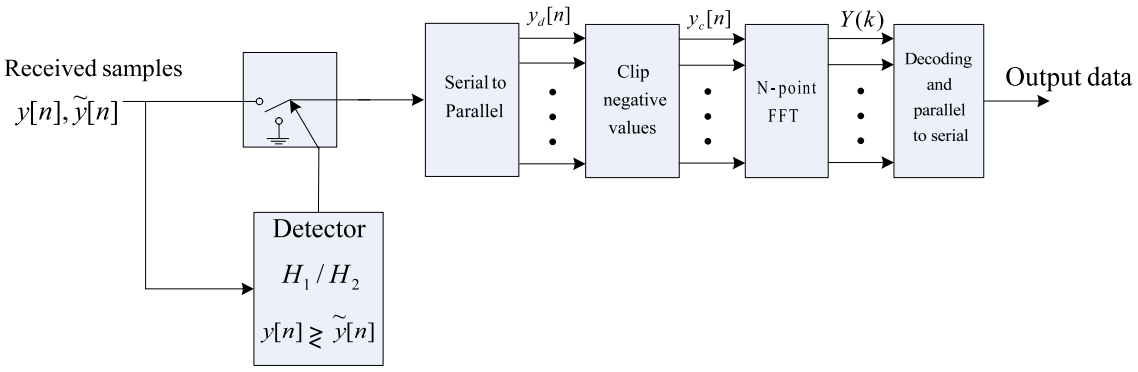

Figure 4.2: Diagram of the proposed improved ACO-OFDM and PAM-DMT receiver.

4.2 Receiver Design

Figure 4.2 presents a block diagram of the proposed receiver which exploits the structure of clipping in ACO-OFDM and PAM-DMT. Novel to this work is the development of a detection element which looks at pairs of incoming samples $y[n]$ and $\tilde{y}[n]$ and selects H_1 or H_2 with maximum likelihood. Once a hypothesis is selected, either $y[n]$ or $\tilde{y}[n]$ is set to zero while the other is left unchanged. In this manner, the technique removes half of the noise power in the received signal and yields output $y_d[n]$. Like [48], $y_d[n]$ is clipped at zero to remove excess noise giving rise to $y_c[n]$. Finally an FFT is performed on $y_c[n]$ and data extracted from the modulated subcarriers. In what follows, the maximum likelihood detector for H_1/H_2 at the receiver is developed.

4.2.1 Joint Distribution of the Received Signal

The joint pdf of the pair $(y[n], \tilde{y}[n])$, for $n = 0, 1, \ldots, N/2 - 1$, is

$$f_{y,\tilde{y}}(y_1, y_2) \;=\; 0.5\; f_{y,\tilde{y}|H_1}(y_1, y_2) + 0.5\; f_{y,\tilde{y}|H_2}(y_1, y_2). \tag{4.11}$$

In order to derive the joint pdf, the conditional pdfs $f_{y,\tilde{y}|H_1}(y_1, y_2)$ and $f_{y,\tilde{y}|H_2}(y_1, y_2)$ are derived first. As an example, for a given n, assume H_1 is true, i.e.,

$$\begin{aligned} y[n] &= x_c[n] + z[n], \\ \tilde{y}[n] &= 0 + \tilde{z}[n] \end{aligned} \tag{4.12}$$

where

$$\tilde{y}[n] = \begin{cases} y[n + N/2] & ; \quad \text{in ACO-OFDM} \\ y[N - n] & ; \quad \text{in PAM-DMT} \end{cases}, \tag{4.13}$$

and

$$\tilde{z}[n] = \begin{cases} z[n + N/2] & ; \quad \text{in ACO-OFDM} \\ z[N - n] & ; \quad \text{in PAM-DMT} \end{cases}. \tag{4.14}$$

Notice that z and $\tilde{z}$ are jointly Gaussian with distribution,

$$f_{z,\tilde{z}}(z_1, z_2) = \frac{1}{2\pi\sigma_z^2\sqrt{1-\rho^2}} \exp\left(-\frac{z_1^2 + z_2^2 - 2\rho z_1 z_2}{2(1-\rho^2)\sigma_z^2}\right), \tag{4.15}$$

where ρ is the correlation coefficient between z and $\tilde{z}$. Note that for flat channels $\rho = 0$. From (4.2), and due to the independence of signal and noise, the joint condition probability arises from the convolution integral,

$$f_{y,\tilde{y}|H_1}(y_1, y_2) = \int_{-\infty}^{\infty}\int_{-\infty}^{\infty} f_{x_c,\tilde{x}_c|H_1}(y_1 - z_1, y_2 - z_2)\ f_{z,\tilde{z}}(z_1, z_2)\ dz_1\ dz_2,$$

(4.16)

which is equal to:

$$f_{y,\tilde{y}|H_1}(y_1,y_2) = \frac{1}{\pi\sqrt{2\pi}\sigma_x\sigma_z^2\sqrt{1-\rho^2}}\int_{-\infty}^{\infty}\int_{-\infty}^{\infty} u(y_1-z_1)\delta(y_2-z_2) \exp\Big(-\frac{(y_1-z_1)^2}{2\sigma_x^2} - \frac{z_1^2+z_2^2-2\rho z_1 z_2}{2(1-\rho^2)\sigma_z^2}\Big)\, dz_1\, dz_2. \tag{4.17}$$

Simplifying (4.17) gives the resulting integral,

$$f_{y,\tilde{y}|H_1}(y_1,y_2) = \frac{1}{\pi\sqrt{2\pi}\sigma_x\sigma_z^2\sqrt{1-\rho^2}}\int_{-\infty}^{y_1} \exp\Big(-\frac{(y_1-z_1)^2}{2\sigma_x^2} - \frac{z_1^2+y_2^2-2\rho z_1 y_2}{2(1-\rho^2)\sigma_z^2}\Big)\, dz_1. \tag{4.18}$$

Solving (4.18) leads to,

$$f_{y,\tilde{y}|H_1}(y_1,y_2) = \frac{\exp\Big(-\frac{y_1^2\sigma_z^2+y_2^2(\sigma_x^2+\sigma_z^2)-2\sigma_z^2\rho y_1 y_2}{2\sigma_z^2(\sigma_x^2+(1-\rho^2)\sigma_z^2)}\Big)\mathrm{erfc}\Big(-\frac{\sigma_x(y_1-\rho y_2)}{\sigma_z\sqrt{2(1-\rho^2)(\sigma_x^2+(1-\rho^2)\sigma_z^2)}}\Big)}{2\pi\sigma_z\sqrt{\sigma_x^2+(1-\rho^2)\sigma_z^2}}, \tag{4.19}$$

in which $\mathrm{erfc}(t)$ is the complementary error function defined as:

$$\mathrm{erfc}(t) = \frac{2}{\sqrt{\pi}}\int_t^{\infty} e^{-u^2}\, du. \tag{4.20}$$

Due to the symmetry of the system, the conditional pdf $f_{y,\tilde{y}|H_2}(y_1,y_2)$ can be obtained from (4.19) by swapping the coordinates y_1 and y_2:

$$\begin{aligned} f_{y,\tilde{y}|H_2}(y_1,y_2) &= f_{y,\tilde{y}|H_1}(y_2,y_1) \\ &= \frac{\exp\Big(-\frac{y_2^2\sigma_z^2+y_1^2(\sigma_x^2+\sigma_z^2)-2\sigma_z^2\rho y_1 y_2}{2\sigma_z^2(\sigma_x^2+(1-\rho^2)\sigma_z^2)}\Big)\mathrm{erfc}\Big(-\frac{\sigma_x(y_2-\rho y_1)}{\sigma_z\sqrt{2(1-\rho^2)(\sigma_x^2+(1-\rho^2)\sigma_z^2)}}\Big)}{2\pi\sigma_z\sqrt{\sigma_x^2+(1-\rho^2)\sigma_z^2}}. \end{aligned} \tag{4.21}$$

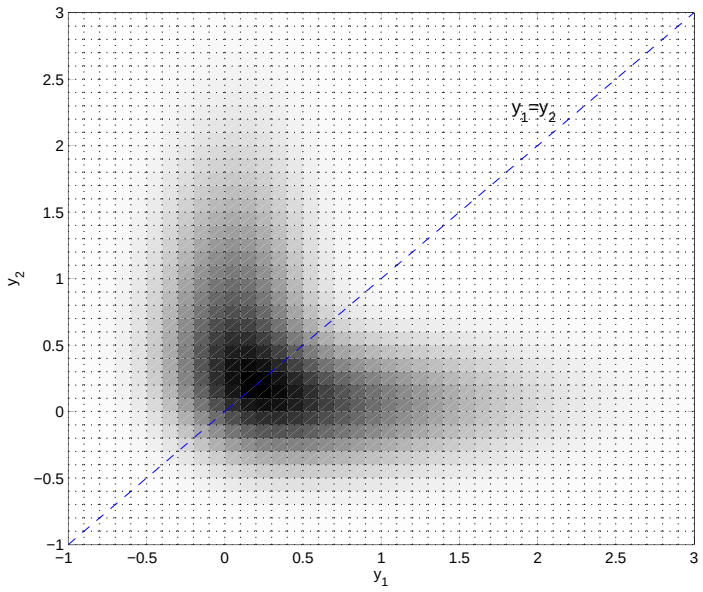

Figure 4.3: The joint *pdf* of the equalized received signal as shown in (4.11), with $\sigma_x^2 = 1$, $\sigma_z^2 = 0.1$, and $\rho = 0.1$.

Replacing the resulting distributions $f_{y,\tilde{y}|H_1}(y_1, y_2)$ and $f_{y,\tilde{y}|H_2}(y_1, y_2)$ in (4.11) yields the joint distribution of the received signal as displayed in Fig. 4.3. Notice that the joint distribution is symmetrical about the line $y_1 = y_2$.

4.2.2 Pairwise Maximum Likelihood Detector

The maximum likelihood detector for H_1 and H_2 takes as input $y[n]$ and $\tilde{y}[n]$ for $n = 0, 1, \ldots, N/2 - 1$ and outputs a decision which minimizes the likelihood of error. Consider a particular pair of received samples at index n, $y[n]$ and $\tilde{y}[n]$. The ML detector selects H_1 when $f_{y,\tilde{y}|H_1}(y[n], \tilde{y}[n]) > f_{y,\tilde{y}|H_2}(y[n], \tilde{y}[n])$, otherwise H_2 is selected. This detector is essentially guessing which of $y[n]$ or $\tilde{y}[n]$ contains a noisy signal and which has only noise. Thus, once a decision is made, the sample which is detected as containing only noise is set to zero.

The form of the ML detector in this case is also particularly simple due to the symmetry in the conditional distributions (4.21). Notice that $f_{y,\tilde{y}|H_1}(y_1, y_2) = f_{y,\tilde{y}|H_2}(y_1, y_2)$ when $y_1 = y_2$. In fact, it is simple to show that

$$f_{Y_1Y_2|H_1}(y_1, y_2) > f_{Y_1Y_2|H_2}(y_1, y_2) \Leftrightarrow y_1 > y_2. \tag{4.22}$$

This can be shown by noting that $\exp(t)$ and $\text{erfc}(-t)$ are increasing functions with respect to t. From (4.19) and (4.21) it can be concluded that:

$$y_1 > y_2 \Rightarrow \begin{cases} \exp(-\frac{y_1^2\sigma_z^2+y_2^2(\sigma_x^2+\sigma_z^2)-2\sigma_z^2\rho y_1 y_2}{2\sigma_z^2(\sigma_x^2+(1-\rho^2)\sigma_z^2)}) > \exp(-\frac{y_2^2\sigma_z^2+y_1^2(\sigma_x^2+\sigma_z^2)-2\sigma_z^2\rho y_1 y_2}{2\sigma_z^2(\sigma_x^2+(1-\rho^2)\sigma_z^2)}), \\ \text{erfc}(-\frac{\sigma_x(y_1-\rho y_2)}{\sigma_z\sqrt{2(1-\rho^2)(\sigma_x^2+(1-\rho^2)\sigma_z^2)}}) > \text{erfc}(-\frac{\sigma_x(y_2-\rho y_1)}{\sigma_z\sqrt{2(1-\rho^2)(\sigma_x^2+(1-\rho^2)\sigma_z^2)}}). \end{cases} \tag{4.23}$$

In other words:

$$y_1 > y_2 \Rightarrow f_{y,\tilde{y}|H_1}(y_1, y_2) > f_{y,\tilde{y}|H_2}(y_1, y_2). \tag{4.24}$$

Similarly, it can be shown that:

$$y_2 > y_1 \Rightarrow f_{y,\tilde{y}|H_2}(y_1, y_2) > f_{y,\tilde{y}|H_1}(y_1, y_2). \tag{4.25}$$

Using (4.24) and (4.25), equation (4.22) can be concluded.

As a result, the ML detector with inputs $y[n]$ and $\tilde{y}[n]$ is simply,

$$\begin{aligned} H_1 &: \text{ if } y[n] > \tilde{y}[n] \\ H_2 &: \text{ otherwise.} \end{aligned}$$

When H_1 is selected then the sample at $\tilde{y}[n]$ is set to zero and $y[n]$ is left unchanged.

Clearly the above detector and zero insertion scheme reduces the noise power. However, the decisions made are not always correct and can ultimately destroy a sample that contains signal. The probability of erroneous detection can be written as

$$\begin{aligned} P_e &= \underbrace{P(y < \tilde{y} \cap x_c > \tilde{x}_c)}_{P_{e_1}} \\ &+ \underbrace{P(y > \tilde{y} \cap x_c < \tilde{x}_c)}_{P_{e_2}} . \end{aligned} \tag{4.26}$$

In (4.26), P_{e_1} and P_{e_2} are the conditional probabilities of erroneous detection given a particular configuration. From the symmetry of the system it can be concluded that

$$P_{e_1} = P_{e_2}.$$

As a result, the probability of erroneous decision is

$$P_e = 2P_{e_1} = 2\int_{-\infty}^{\infty}\int_{-\infty}^{y_2} f_{y,\tilde{y}|H_1}(y_1, y_2)\ dy_1\ dy_2. \tag{4.27}$$

Notice also that the probability of correct detection is equal to:

$$P_c = 1 - P_e. \tag{4.28}$$

In the next section, the bit-error rate (BER) versus the optical signal to noise ratio is simulated for flat and non-flat channels and different receiver designs.

4.3 Simulations and Results

For all simulations, $N = 1024$ subcarriers are considered where 16-QAM is used to load data into the odd frequency bins of ACO-OFDM, and 4-PAM is used to modulate imaginary parts of the subcarriers in PAM-DMT. In order to compare the performance of the proposed pairwise ML receiver, several previously proposed designs are also simulated. As a baseline, the receiver in [44] is simulated where data is only extracted from the modulated subcarriers ("No Detection"). The receiver in [48] is also simulated where all received samples are clipped prior to FFT ("Clip Only"). The receiver with pairwise ML detector presented in Sec. 4.2.2 is denoted "ML with Clip". Finally, a genie receiver is simulated in which the detector make perfect decisions in zeroing samples of $y[n]$ and is denoted "Genie Rx with Clip". Simulations are repeated for the case of a flat channel and a lowpass channel response.

4.3.1 Performance of ACO-OFDM and PAM-DMT in Flat Channels

The error performance of different receivers for ACO-OFDM and PAM-DMT in flat channels are presented in Fig. 4.4. As can be seen, the receiver of [44] with no detection has the worst performance in terms of BER. Also, the clip only receiver of [48] has a slightly better performance. By using the anti-symmetry of the signal in ML receiver, approximately 1.3 dB optical gain is achieved at $BER = 10^{-5}$ compared to no detection receiver. Notice also that the genie receiver has the best performance since it always makes the correct decision, thus removes half the noise power yielding a gain of about 1.5 dB in SNR_o over the no detection case. Simulation results indicate

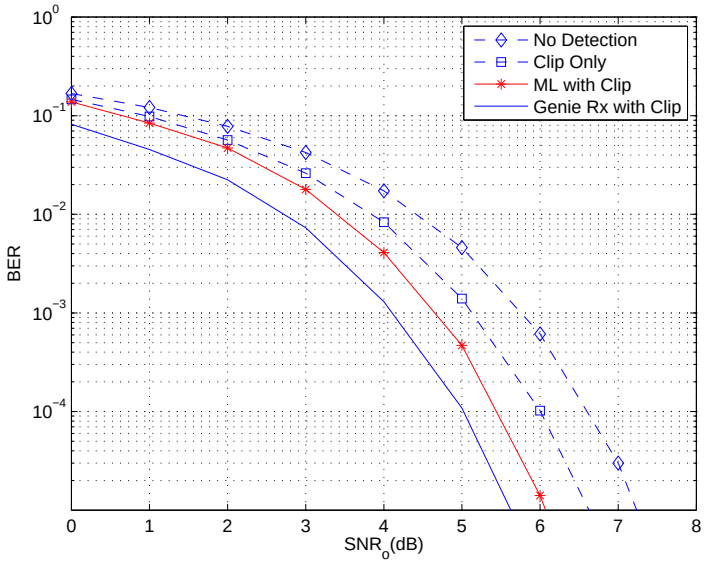

Figure 4.4: BER versus SNR for different ACO-OFDM and PAM-DMT receiver designs in flat channels ($\rho = 0$).

that the performance of ACO-OFDM and PAM-DMT is identical on flat channels.

The probability of erroneous detection in (4.27) versus SNR_o is shown in Fig. 4.5 for a frequency flat channel, i.e. the noise is white Gaussian distributed and $\rho = 0$. Notice that at $SNR_o = 6$ dB the that the $BER \approx 10^{-5}$ in Fig. 4.4 while about 7% of decisions are incorrect. Thus, in spite of the erroneous detection errors in the pairwise ML detector, the loss of signal power is small and a significant gain is still achieved.

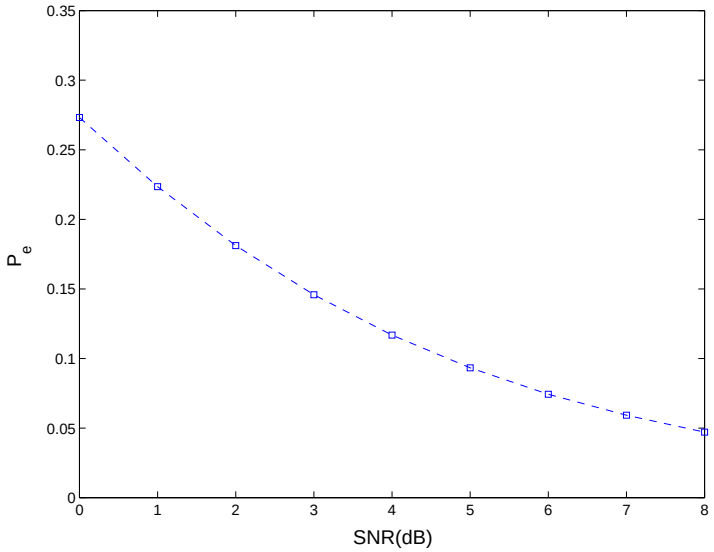

Figure 4.5: Probability of erroneous decision for ACO-OFDM and PAM-DMT pairwise ML receiver in flat channels ($\rho = 0$).

4.3.2 Performance of ACO-OFDM and PAM-DMT in a Lowpass Channel

As an example of a lowpass channel, a Gaussian channel in frequency with 3-dB cut-off at the end of the frequency spectrum is assumed with transfer function

$$H[k] = \exp\left(-\frac{k^2}{2\sigma_H^2 N^2}\right), k = 0, 1, \ldots, \frac{N}{2} - 1, \tag{4.29}$$

where $\sigma_H^2 = 0.1803$ which puts the 3-dB frequency at the end of the transmit spectrum.

Figure 4.6 and 4.7 display the error performance of an ACO-OFDM and PAM-DMT systems on a Gaussian channel of (4.29). Similar to flat channels, it can be seen that the pairwise ML receiver outperforms the conventional receivers and has a gain of about 1 dB in SNR_o over the conventional ACO-OFDM and PAM-DMT detector

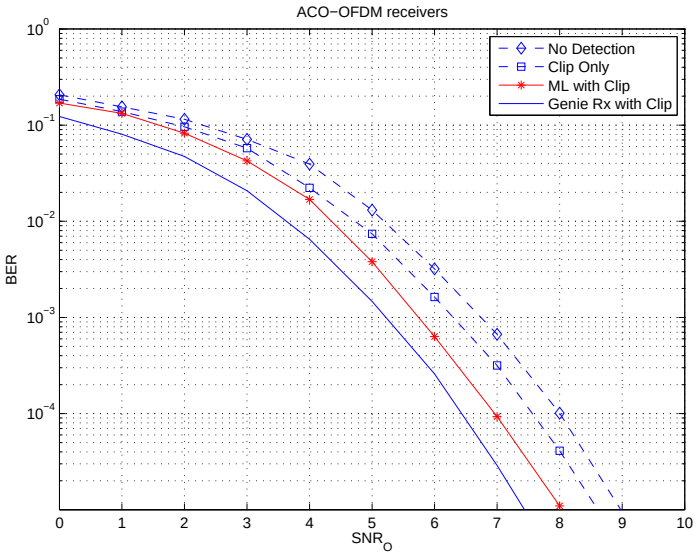

Figure 4.6: BER versus SNR for different ACO-OFDM receiver designs in a low-pass Gaussian channel in frequency.

in [44]. Notice that this gain is smaller than in the flat channel. This is due to the fact that the detector is only *pairwise* ML and does not take into account the significant correlation of the noise samples. However, as an advantage, the pairwise ML detector is very simple to implement. Notice also that the performance of PAM-DMT in this channel is slightly better compared to ACO-OFDM. This is due to the difference in the correlation between the noise samples in ACO-OFDM and PAM-DMT.

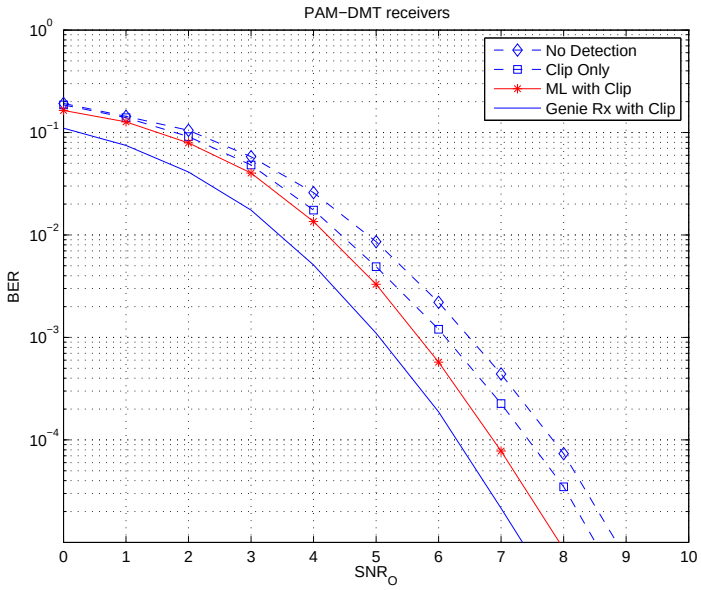

Figure 4.7: BER versus SNR for different PAM-DMT receiver designs in a low-pass Gaussian channel in frequency.

4.4 Conclusions

In this chapter, the properties of ACO-OFDM and PAM-DMT systems are formalized. It is shown that by using the anti-symmetry of the time domain samples, the joint distribution of the received signal can be found and used to devise a new detector. Hence, a new receiver design for ACO-OFDM and PAM-DMT systems is proposed and simulated. The receiver exploits the anti-symmetry of the time samples inherent in such systems and further increases its optical power efficiency. Gains are quantified in simulation and on flat channels provide at least 1.3 dB gain at $BER = 10^{-5}$.

Chapter 5

Conclusions and Future Work

5.1 Conclusions

A main contribution of this thesis is the introduction of a novel orthogonal frequency division multiplexing (OFDM) scheme for optical communication systems termed as *spectrally factorized optical* OFDM (SFO-OFDM). The drawbacks of the previous compatible OFDM methods for non-negative, intensity modulated direct detection (IM/DD) optical channels are mitigated in the proposed SFO-OFDM scheme.

By spectrally factorizing the non-negative band-limited periodic time signals, a framework for designing an optical OFDM compatible scheme is derived. Instead of directly modulating the sub-carriers, the autocorrelation of the complex data sequence is performed before transmission to guarantee non-negativity. Unlike asymmetrically clipped optical OFDM (ACO-OFDM) and pulse amplitude modulated discrete multi-tone (PAM-DMT), the proposed SFO-OFDM system does not require reversed sub-carriers. Furthermore, the non-negativity of the time signal is already guaranteed by spectrally factorizing the signal. Hence there is no need for external bias source

unlike DC-biased OFDM. The proposed method has improvement both in optical power efficiency and peak-to-average-power ratio.

Also in this thesis, a new maximum likelihood detection scheme for ACO-OFDM and PAM-DMT receivers is proposed. The conventional receivers ignore the structure of the clipping noise in detection. The new detector exploits the inherent anti-symmetry structure of the time samples in ACO-OFDM and PAM-DMT to remove half the noise power at the receiver. The proposed detection scheme is simulated and shown to improve the optical power efficiency of the system.

5.2 Future Work

The SFO-OFDM model can be extended to incorporate a peak amplitude constraint. Notice that $x(t) > 0$ implies that the zeros of characteristic function $T_1(z)$ appear in conjugate reciprocal pairs $\lambda_i, 1/\lambda_i^*$ where λ_i are located outside the unit circle. Assume the peak constraint be formulated as,

$$x(t) < A, \tag{5.1}$$

which is equivalent to,

$$s(t) = A - x(t) > 0. \tag{5.2}$$

Therefore, the zeros of characteristic function of $s(t)$, denoted by $T_2(z)$, are also in conjugate reciprocal pairs $\gamma_i, 1/\gamma_i^*$ where γ_i are located outside the unit circle and,

$$\gamma_i = f_i(\lambda_1, \lambda_2, \cdots, \lambda_K, A). \tag{5.3}$$

In order to find the relation between the zeros of $T_1(z)$ and $T_2(z)$, their spectral factorization can be used. Notice that:

$$\begin{aligned} T_1(z) &= S_1(z)\ S_1^*\left(\frac{1}{z^*}\right), \\ T_2(z) &= S_2(z)\ S_2^*\left(\frac{1}{z^*}\right). \end{aligned} \tag{5.4}$$

Notice also that if a_l and b_l denote the Fourier series coefficients of $x(t)$ and $s(t)$, then:

$$b_l = \begin{cases} -a_l & \text{if } l \neq 0 \\ A - a_0 & \text{if } l = 0. \end{cases} \tag{5.5}$$

Consequently,

$$T_2(z) = A - T_1(z). \tag{5.6}$$

Using (3.10), equation (5.6) can be formulated as follows,

$$\underbrace{\left(\frac{c_2\ (-1)^K}{\prod_{i=1}^{K}(\gamma_i^*)}\right)}_{c_2'}\prod_{i=1}^{K}(1-\gamma_i z^{-1})\prod_{i=1}^{K}(1-\gamma_i^* z) =$$

$$A-\underbrace{\left(\frac{c_1\ (-1)^K}{\prod_{i=1}^{K}(\lambda_i^*)}\right)}_{c_1'}\prod_{i=1}^{K}(1-\lambda_i z^{-1})\prod_{i=1}^{K}(1-\lambda_i^* z), \tag{5.7}$$

where c_1 and c_2 are chosen such that c_1' and c_2' are positive. By appropriate choice of c_1 and c_2, equating the coefficients of z^l for all $l \in \{-K, \cdots, K\}$, and solving the set of equalities, the relation between γ_i and λ_i can be found as in (5.3).

Solving the inequality $\|\gamma_i\| = \|f(\lambda_i, A)\| > 1$, will specify a region R for the places of λ_i. If the λ_i are chosen from the region of R which is outside the unit circle, both non-negativity and peak constraint will be satisfied simultaneously.

There is room for improvement in the SFO-OFDM design presented in this thesis and the mentioned results are only the first design schemes. Works can be done to reduce the order of complexity in the structure of the receiver. Furthermore, instead of locating the zeros on the fixed radius ring, optimization techniques can be used to guide the zero places.

Bibliography

[1] J. R. Barry, *Wireless infrared communications*. Kluwer Academic Press, Boston, MA, 1994.

[2] S. S. Muhammad, P. Kohldorfer, and E. Leitgeb, "Channel modeling for terrestrial free space optical channels," in *Proceedings of the International Conference on Transparent Optical Networks*, vol. 1, pp. 407–410, July 2005.

[3] Z. Xu and B. M. Sadler, "Ultraviolet communications: Potential and state-of-the-art," *IEEE Communications Magazine*, vol. 46, pp. 67–73, May 2008.

[4] R. D. Dupuis and M. R. Krames, "History, development, and applications of high-brightness visible light-emitting diodes," *Journal of Lightwave Technology*, vol. 26, May 2008.

[5] Visible spectrum. (2010). [Online]. Available: http://en.wikipedia.org.

[6] D. A. Steigerwald, J. C. Bhat, D. Collins, R. M. Fletcher, M. O. Holcomb, M. J. Ludowise, P. S. Martin, and S. L. Rudaz, "Illumination with solid state lighting technology," *IEEE journal of Selected Topics in Quantum Electronics*, vol. 8, pp. 310–320, April 2002.

[7] J. N. Holonyak, "Is the light emitting diode (LED) an ultimate lamp?," *J. Phys.*, vol. 68, pp. 864–866, September 2000.

[8] Comparison Chart LED Lights vs. Incandescent Light Bulbs vs. CFLs. [Online]. Available: http://www.designrecyacleinc.com.

[9] STARLIGHT LED. [Online]. Available: http://www.ledstarlight.com.

[10] T. P. Lee and A. G. Dentai, "Power and modulation bandwidth of gaas-algaas high-radiance led's for optical communication systems," *IEEE Journal of Quantum Electronics*, vol. 14, pp. 150–159, March 1987.

[11] T. Komine and M. Nakagawa, "Fundamental analysis for visible-light communication systems using LED lights," *IEEE Transaction on Consumer Electronics*, 2004.

[12] VLCC: Visible Light Communication Consortium. (2008). [Online]. Available: http://www.vlcc.net.

[13] T. Komine and M. Nakagawa, "Integrated system of white LED visible light communication and power-line communication," in *IEEE Transactions on Consumer Electronics*, vol. 49, February 2003.

[14] Project OMEGA. [Online]. Available: www.ict-omega.eu.

[15] O. Bouchet, M. E. Tabach, M. Wolf, D. C. O'Brien, G. E. Faulkner, J. W. Walewski, S. Randel, M. Franke, S. Nerreter, K. D. Langer, J. Grubor, and T. Kamalakis, "Hybrid wireless optics (HWO): building the next-generation home network," in *IEEE CSNDCP*, pp. 283–287, 2008.

[16] Forum, W. W. R.: Wireless World Research Forum, (2008). [Online]. Available: http://www.wireless-world-research.org/?id=92.

[17] P. Amirshahi and M. Kavehrad, "Broadband access over medium and low voltage power-lines and use of white light emitting diodes for indoor communications," in *Consumer Communications and Networking Conference (CCNC)*, vol. 2, 2006.

[18] Visible Light Communication: USA. [Online]. Available: http://www.lvx-system.com/.

[19] Boston University Smart Lighting Center. [Online]. Available: http://www.bu.edu/smartlighting/.

[20] Japan Electronics and Information Technology Industries Association (JEITA). [Online]. Available: http://www.jeita.or.jp.

[21] JEITA:'CP-1221 Visible Light Communication System',2007.

[22] JEITA:'CP-1222 Visible Light ID System',2007.

[23] IEEE 802.15 WPAN Visual Light Communication Interest Group (IGvlc) [Online]. Available: http://www.ieee802.org/15/pub/IGvlc.html, 2008.

[24] J. Grubor, O. C. G. Jamett, J. W. Walewski, S. Randel, and K.-D. Langer, "High-speed wireless indoor communication via visible light," *ITG Fachbericht*, pp. 203–208, 2007.

[25] D. O'Brien, H. L. Minh, L. Zeng, G. Faulkner, K. Lee, D. Jung, Y. Oh, and E. T. Won, "Indoor visible light communications: Challenges and prospects," *Proceedings SPIE*, vol. 7091, 2008.

[26] H. L. Minh, D. O'Brien, G. Faulkner, L. Zeng, K. Lee, D. Jung, and Y. Oh, "High-speed visible light communications using multiple-resonant equalization," *IEEE Photonic Technology Letters*, vol. 20, July 2008.

[27] J. Grubor, S. C. J. Lee, K.-D. Langer, T. Koonen, and J. W. Walewski, "125 Mbit/s over 5 m wireless distance by use of OOK-modulated phosphorescent white LEDs," in *European Conference and Exhibition on Optical Communication (ECOC)*, 2009.

[28] J. Vucic, C. Kottke, A. Buttner, K. D. Langer, and J. W. Walewski, "White-light wireless transmission at 200+ Mbit/s net data rate by use of discrete-multitone modulation," *IEEE Photonics Technology Letters*, vol. 21, October 2009.

[29] L. Zeng, D. C. O'Brien, H. L. Minh, G. E. Faulkner, K. Lee, D. Jung, Y. Oh, and E. T. Won, "High data rate multiple input multiple output (MIMO) optical wireless communications using white LED lighting," *IEEE Journal on Selected Areas in Communications*, vol. 27, December 2009.

[30] D. O'Brien, L. Z. nd H. Le-Minh, G. Faulkner, and J. W. Walewski, "Visible light communications: Challenges and possibilities," in *19th International Symposium on Indoor and Mobile Radio Communications (PIMRC) 2008*, September 2008.

[31] T. Komine, S. Haruyama, and M. Nakagawa, "Bidirectional visible light communication using corner cube modulator," in *Proc. Wireless and Optical Communications (WOC). Banff, Canada. IASTED*, July 2003.

[32] J. Hou and D. C. O'Brien, "Vertical handover-decision-making algorithm using

fuzzy logic for the integrated Radio-and-OW system," *IEEE Transactions on Wireless Communications*, no. 176-185, 2006.

[33] H. B. C. Wook, T. Komine, S. Haruyama, and M. Nakagawa, "Visible light communication with LED-based traffic lights using 2-dimensional image sensor," in *IEEE Consumer Communications and Networking Conference (CCNC)*, vol. 1, 2006.

[34] G. Pang, T. Kwan, H. Liu, and C.-H. Chan, "A novel use of LEDs to transmit audio and digital signals," *IEEE Ind. Appl. Mag.*, vol. 8, no. 1, pp. 21–28, 2002.

[35] Audi corporation. [Online]. Available: http://www.audi.ca/ca/brand/en/models/r8.html.

[36] K.-D. Langer and J. Grubor, "Recent developments in optical wireless communications using infrared and visible light," in *9th International Conference on Transparent Optical Networks*, vol. 3, July 2007.

[37] Visible light communication system: Nakagawa Group. [Online]. Available: http://www.youtube.com/watch?v=QEh5f49LsB4.

[38] Geospatial Information Authority of Japan. [Online]. Available: http://www.gsi.go.jp/ENGLISH/.

[39] Communication in transportation systems. [Online]. Available: http://www.inatel.br/iwt/slide-show/communication-in-transportation-systems.

[40] Y. Ito, S. Haruyama, and M. Nakagawa, "Rate-adaptive transmission on a wavelength dependent channel for underwater wireless communication using visible light LEDs," vol. 105, pp. 127–132, February 2006.

[41] Underwater visible light communications. [Online]. Available: http://www.youtube.com/watch?v=vvjTFoDnfEU.

[42] H. Guo-yong, C. Chang-ying, and C. Zhen-qiang, "Free-space optical communication using visible light," *Journal of Zheijiang University*, 2007.

[43] J. M. Kahn and J. R. Barry, "Wireless infrared communications," *Proceedings of IEEE*, vol. 85, February 1997.

[44] J. Armstrong and A. J. Lowery, "Power efficient optical OFDM," *Electronics Letters*, vol. 42, pp. 370–372, March 2006.

[45] J. Armstrong and B. J. C. Schmidt, "Comparison of asymmetrically clipped optical OFDM and DC-biased optical OFDM in AWGN," *IEEE Communications Letters*, vol. 12, May 2008.

[46] J. Armstrong, B. J. C. Schmidt, D. Kalra, H. A. Suraweera, and A. J. Lowery, "Performance of asymmetrically clipped optical OFDM in AWGN for an intensity modulated direct detection system," in *IEEE Global Telecommunications Conference, 2006. GLOBECOM*, 2006.

[47] X. Liu, R. Mardling, and J. Armstrong, "Channel capacity of IM/DD optical communication systems and of ACO-OFDM," in *IEEE International Conference on Communications ICC*, 2007.

[48] S. K. Wilson and J. Armstrong, "Transmitter and receiver methods for improving asymmetircally-clipped optical OFDM," *IEEE Transactions on Wireless Communications*, vol. 8, September 2009.

[49] S. C. J. Lee, S. Randel, F. Breyer, and A. M. J. Koonen, "PAM-DMT for intensity-modulated and direct-detection optical communication systems," *IEEE Photonic Technology Letters*, vol. 21, December 2009.

[50] K. Asadzadeh, A. A. Farid, and S. Hranilovic, "Spectrally factorized optical OFDM," in *12th Canadian Workshop on Information Theory (CWIT)*, 2011.

[51] K. Asadzadeh, A. Dabbo, and S. Hranilovic, "Receiver design for asymmetrically clipped optical OFDM," to appear in the *2nd IEEE Globecom Workshop on Optical Wireless Communications*, 2011.

[52] S. Hranilovic, *Wireless Optical Communication Systems*. Kluwer Academic Publisher, 2005.

[53] J. Grubor, S. Randel, K.-D. Langer, and J. W. Walewski, "Broadband information broadcasting using LED-based interior lighting," *Journal of Lightwave technology*, vol. 26, December 2008.

[54] IEEE 802.15 TG7. [Online]. Available: http://www.ieee802.org/15/pub/TG7.html.

[55] Light-emitting diode. [Online]. Available: http://en.wikipedia.org.

[56] OSRAM LEDs. [Online]. Available: http://www.osram-os.com.

[57] PHILIPS LEDs. [Online]. Available: http://www.lighting.philips.com.

[58] Personic LEDs. [Online]. Available: http://www.bcledlights.com.

[59] NICHIA LEDs. [Online]. Available: http://www.nichia.com.

[60] VISHAY LEDs. [Online]. Available: http://www.vishay.com/leds.

[61] L. Harrington, C. Bassi, and C. Peck, "Luminous efficiency and the measurement of luminous efficiency and the measurement of daytime displays, signals, and visors," *Aviation, Space, and Environmental Medicine*, vol. 76, no. 5, 2005.

[62] Technical datasheet DS23. [Online]. Available: http://www.dotlight.de.

[63] International Organization for Standardization. [Online]. Available: http://www.iso.org.

[64] International Electrotechnical Commission. [Online]. Available: www.iec.ch.

[65] T. P. Lee, "The nonlinearity of double-heterostructure LEDs for optical communications," *Proceedings of IEEE*, vol. 65, no. 9, pp. 1408–1410, 1977.

[66] B. Inan, S. C. J. Lee, S. Randel, I. Neokosmidis, A. M. J. Koonen, and J. W. Walewski, "Impact of LED nonlinearity on discrete multitone modulation," *Journal of Optical Society America*, vol. 1, October 2009.

[67] V. Jungnickel, V. Pohl, S. Nonnig, and C. von Helmolt, "A physical model of the wireless infrared communication channel," *IEEE Journal on Selected Areas in Communications*, vol. 20, April 2002.

[68] A. J. C. Moreira, R. T. Valadas, and A. de Oliveira Duarte, "Optical interference produced by artificial light," *Wireless Networks*, pp. 131–140, 1997.

[69] D. L. Rogers, "Integrated optical receivers using MSM detectors," *Journal of Lightwave Technology*, vol. 9, pp. 1635–1638, December 1991.

[70] J. B. Carruthers and J. M. Kahn, "Multiple-subcarrier modulation for non-directed wireless infrared communication," *IEEE Journal on Selected Areas in Communications*, vol. SAC-14, pp. 538–546, April 1996.

[71] M. Z. Afgani, H. Haas, H. Elgala, and D. Knipp, "Visible light communication using OFDM," in *2nd International Conference on Testbeds and Research Infrastructure for the Development of Networks and Communities*, 2006.

[72] T. Komine, S. Haruyama, and M. Nakagawa, "Performance evaluation of narrowband OFDM on integrated system of power line communication and visible light communication," in *1st International Symposium on Wireless Pervasive Computing*, January 2006.

[73] H. Elgala, R. Mesleh, H. Haas, and B. Pricope, "OFDM visible light communication based on white LEDs," in *65th Vehicular Technology Conference*, April 2007.

[74] J. Grubor, S. C. J. Lee, K. D. Langer, T. Koonen, and J. W. Walewski, "Wireless high speed data transmission with phosphorescent white light LEDs," in *33rd European Conference and Exhibition of Optical Communication (ECOC), Berlin, Germany*, 2007.

[75] S. Hranilovic, "On the design of bandwidth efficient signalling for indoor wireless optical channels," *International Journal of Communication Systems*, vol. 18, pp. 205–228, 2005.

[76] O. Gonzalez, R. Perez-Jimenez, S. Rodriguez, J. Rabadan, and A. Ayala,

"OFDM over indoor wireless optical channel," *Optoelectronics, IEE Proceedings*, vol. 152, pp. 199–204, 2005.

[77] S. Teramoto and T. Ohtsuki, "Multiple-subcarrier modulation optical communication systems with subcarrier signal-point sequence," *IEEE Transactions on Communications*, vol. 53, pp. 1738–43, 2005.

[78] N. E. Jolley, H. Kee, P. Pickard, J. Tang, and K. Cordina, "Generation and propagation of a 1550 nm 10 Gbit/s optical orthogonal frequency division multiplexed signal over 1000m of multimode fibre using a directly modulated DFB," in *Optical Fiber Communication Conference (OFC), 6-11 March 2005, Anaheim, CA, USA*, 2005.

[79] J. M. Tang, P. M. Lane, and K. A. Shore, "Transmission performance of adaptively modulated optical OFDM signals in multimode fiber links," *IEEE Photonic Technology Letters*, vol. 18, pp. 205–207, 2006.

[80] N. Kitamoto and T. Ohtsuki, "Parallel combinatory multiple-subcarrier optical wireless communication systems," *International Journal of Communication Systems*, vol. 18, pp. 195–203, 2005.

[81] C. Babla, "Addressing challenges in serial 10 Gb/s multimode fiber enterprise networks," *IEEE Communications Magazine*, vol. 43, pp. 22–28, 2005.

[82] K. R. Panta and J. Armstrong, "Effects of clipping on the error performance of OFDM in frequency selective fading channels," *IEEE Transactions on Wireless Communications*, vol. 3, pp. 668–71, 2004.

[83] A. F. Molisch, M. Z. Win, and J. H. Winters, "Space-time-frequency (STF) coding for MIMO-OFDM systems," *IEEE Communications Letters*, vol. 6, pp. 370–72, September 2002.

[84] J. Tellado, *Multicarrier modulation with low PAR: applications to DSL and wireless*. Kluwer Academic Publisher, MA, USA, 2000.

[85] S. P. Wu, S. Boyd, and L. Vandenberghe, "FIR filter design via spectral factorization and convex optimization," *Applied and Computational Control, Signals and Circuits*, vol. 1, 1999.